UC Berkeley
UC Berkeley Previously Published Works

Title

Mixed potential model for passivity characters of hyper-duplex stainless steel 2707 in ammonium carbonate solution containing chloride

Permalink

https://escholarship.org/uc/item/15v8d7vr

Authors

Sun, Li
Zhao, Tianyu
Qiu, Jie
et al.

Publication Date

2022-06-01

DOI

10.1016/j.corsci.2022.110302

Peer reviewed

eScholarship.org Powered by the California Digital Library
University of California

Corrosion Science 201 (2022) 110302

Contents lists available at ScienceDirect

Corrosion Science

journal homepage: www.elsevier.com/locate/corsci

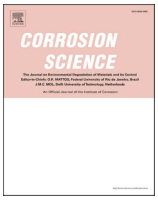

Mixed potential model for passivity characters of hyper-duplex stainless steel 2707 in ammonium carbonate solution containing chloride

Li Sun [a,b,c], Tianyu Zhao [b,e], Jie Qiu [b,d], Yangting Sun [c,*], Weihua Li [a], Haibing Zheng [a], Zhifeng Lin [a], Si Chen [a], Yiming Jiang [c], Jin Li [c], Digby D. Macdonald [b,*]

[a] School of Chemical Engineering and Technology, Sun Yat-sen University, Zhuhai 519082, China
[b] Department of Nuclear Engineering, University of California at Berkeley, Berkeley, CA 94720, United States
[c] Department of Materials Science, Fudan University, Shanghai 200433, China
[d] School of Nuclear Science and Technology, Xi'an Jiaotong University, Xi'an 710049, China
[e] School of Chemical Engineering, Northwest University, Xi'an 710069, China

ARTICLE INFO

Keywords:
HDSS 2707
Point defect model
Mixed potential model
Passivity
Applied potential

ABSTRACT

A mixed potential model (MPM) comprising the Point Defect Model (PDM) and the Generalized Butler Volmer Equation (GBVE) was successfully developed to study the passivity of HDSS 2707. The results show that the dominant point defect within the passive film is the M_i^{n+}, thereby rendering n-type semiconductor behavior of the barrier layer. The anodic current is independent of the film formation potential whereas it increases with increasing temperature and follows the Arrhenius law. The partial cathodic current of hydrogen reaction is affected by the applied voltage. The anodizing constant of the passive film is calculated to be 2.91 nm/V.

1. Introduction

Hyper-duplex stainless steel 2707 (HDSS 2707) is favored as a competitive alternative to expensive super austenitic stainless steels and nickel-based alloys, because of its superb corrosion resistance and attractive mechanical properties [1–5]. The corrosion resistance of HDSS 2707 strongly relies on a balanced two-phase microstructure, and the distribution of alloying elements in both the ferrite and austenite [6]. Our previous research revealed that a desirable corrosion resistance of HDSS 2707 is achieved at the annealing temperature of 1100 ℃ [7]. As known, the low corrosion rate of stainless steels in aqueous environment arises from the existence of a thin passivating oxide film on their surfaces [8]. The passive film formed on HDSS 2707 surface is more stable than those on other duplex stainless steels [9–11], since its breakdown potential (E_b) in 1 M NaCl solution is greater than 0.8 V_{SCE}, which is higher than the oxygen evolution potential; and its critical pitting temperature (CPT) in 3 M NaCl solution is higher than 98 ℃ [7]. These two electrochemical parameters are measured from potentiodynamic and potentiostatic polarization experiments, which are the general methods that are employed for exploring the pitting performance of HDSS 2707, but the data frequently lack direct interpretation with respect to the specific characteristics of the passive film. Literature reviews indicate that the protectiveness of the passive film and its breakdown are critical aspects of pitting corrosion [12–15]. Previously, we have interpreted the pitting parameters of HDSS 2707 in terms of the Point Defect Model (PDM) [16], whereas the other key corrosion factors, including the effect of temperature and applied potential on the oxide film properties, such as the defect concentration, the defect type, the dissolution current density, the corrosion rate (μm/year), and the growth rate of the passive film formed on HDSS 2707 surface are still unknown.

HDSS 2707 is designed to use in petrochemical systems, an aqueous solution containing a mass of NH_3 [17,18], CO_2 [19] and a small amount of chloride [20]. The simulant is defined as various mixtures of $(NH_4)_2CO_3$ + NaCl and is employed to reproduce the corrosive environment for HDSS 2707 in heat exchanger system [21,22]. Therefore, the naturally formed passive film on the steel surface protects the substrate from localized corrosion and effectively prolongs the life span of the equipment. However, aggressive anions, such as chloride, can induce passivity breakdown events on HDSS 2707, as well as accelerating the corrosion rate of the alloy, and finally result in perforation accidents due to pitting. The PDM postulates that the passive film formed on the steel surface comprises two layers, i.e., a dense, point defective, and protective barrier layer (bl) that grows into the metal

* Corresponding authors.
E-mail addresses: sunyangting@fudan.edu.cn (Y. Sun), macdonald@berkeley.edu (D.D. Macdonald).

https://doi.org/10.1016/j.corsci.2022.110302
Received 18 November 2021; Received in revised form 9 March 2022; Accepted 3 April 2022
Available online 6 April 2022
0010-938X/© 2022 Elsevier Ltd. All rights reserved.

Table 1
Chemical composition of HDSS 2707.

Element	Cr	Ni	Mo	N	C	Mn	Cu	S	P	Fe
wt%	26.99	6.48	4.89	0.36	0.017	1.00	0.13	0.001	0.017	bal

Table 2
Composition of the test solution and its measured pH and OCP, and the calculated equilibrium potential of the HER at different temperatures.

Solution	T/ ℃	Measured pH	OCP/ V_{SCE}	V_{eq} (V_{SHE})	V_{eq} (V_{SCE})
0.2 M $(NH_4)_2CO_3$ + 0.1 M NaOH + 0.1 M NaCl	30	13.19	-0.383	-0.751	-0.995
	40	12.87	-0.402	-0.756	-1.000
	50	12.69	-0.445	-0.769	-1.013
	60	12.52	-0.479	-0.783	-1.027

substrate and a precipitated porous outer layer (ol) that forms via the hydrolysis of cations transmitted through the bl and their subsequent reaction with components in the environment. The bl provides a transmission path for the point defects including cation vacancies ($V_M^{\chi'}$), oxygen vacancies ($V_o^{\cdot}$), and cation interstitials ($M_i^{\chi+}$) that are generated and annihilated at the bl interfaces [23,24]. Because of a high electric field (ε) that exists within the bl (1 ~ 3 MV/cm), these defects are transported across the bl by migration rather than by diffusion [25]. Focusing on the cation vacancy ($V_M^{\chi'}$), when the flux rate (J_{ca}) of this defect is higher than that of the annihilation rate (J_m) at the metal/bl (m/bl) interface, the excess cation vacancies condense on the metal lattice or on the cation sublattice of the bl, thereby preventing the growth of the bl into the metal at that location. However, the bl continues to dissolve at the bl/solution interface with the result that the bl thins and ruptures under the developing growth stresses [26]. That marks a passivity breakdown event.

Many factors play important roles in determining this passive state for the stainless steels in aqueous solutions, including the alloying elements (e.g., Mo and Cr), Cl^- concentration, temperature, pH and applied potential. The interplay of the dynamical properties of the passive film formed on the metal surface can be described by the process of point defect reactions, such as the rate constants (k_i), the standard rate constants (k_i^0), the transfer coefficients (α_i), the diffusion coefficient (D), J_m, and J_{ca} at the m/bl interface [27,28]. These kinetic parameters can be determined by optimizing the PDM on electrochemical impedance spectroscopic (EIS) data [29], and some of them have been incorporated into our previous research related to pitting of HDSS 2707 [16].

EIS is a non-destructive, perturbative technique, in which the applied perturbation is of small amplitude sinusoidal voltage, ensuring that the electrochemical state of the electrode is barely changed [30,31]. Thus, it provides the desired electrochemical information about the corrosion kinetics of passive film formed on HDSS 2707 surface with minimal change of the system [32,33]. An innovative mixed potential model (MPM) combining the PDM to describe the partial anodic reactions of the metal dissolution at the atomic level, and the generalized Butler-Volmer equation (GBVE) to describe the cathodic process has been successfully developed and optimized on the experimental EIS data, which allows us to interpret the passivation properties of the oxide film [34,35]. The optimized parameters include the concentrations of the vacancies (C_i^0, $C_{V_0}^0$), the bl and ol resistance ($\Omega \cdot cm^2$), the net anodic current density (i_{ss}), cathode current density (i_c), the film thickness (L_{ss}) and the rate constants (k_i) of the defect reactions as mentioned above. The obtained data are used here to understand the correlations between the corrosion resistance of HDSS 2707 and the characteristics of the passive film.

2. Experimental

HDSS 2707 plate, provided by Sandvik company, was cut into specimens with a dimensions of 12 × 6 × 2 mm. The chemical composition is listed in Table 1, which was determined by chemical analysis. The as-received coupons were first annealed under the atmosphere of pure N_2 at 1100 ℃ for half an hour to achieve homogeneity before quenching in water [7]. The samples were mounted in epoxy resin, and were abraded to 2000 grit with emery paper, then polished with 1.5 μm diamond paste, followed by ultrasonic cleaning in acetone, alcohol, and deionized water.

The simulated buffer solution used in this study is 0.2 M $(NH_4)_2CO_3$ + 0.1 M NaCl, adjusting with 0.1 M NaOH to yield pH = 13 ± 0.2 at 30 ℃. The measured pH in the solution at different temperatures are listed in Table 2. The temperature of the electrolyte ranging from 30 ℃ to 60 ℃ was controlled by a water bath. Before each experiment, the solution was purged with ultrahigh purity N_2 + 4% H_2 (UHP; 99.999%) for at least 3 h to expel oxygen. The hydrogen was added to establish a known, fixed value for the equilibrium potential for the hydrogen electrode reaction (HER), which represents the partial cathodic process and which is used in the optimization analysis. The concentration of hydrogen in solution after bubbling with N_2 + H_2 (4%) is approximately 6.83×10^{-4} cm^3/g (3.0×10^{-5} M) at 30 ℃.

A traditional three-electrode, double-wall cell with a capacity of 300 ml was used for this study. The cell contained a platinum foil as the counter electrode (CE), a saturated calomel electrode as the reference electrode (RE), and a HDSS 2707 specimen as the working electrode (WE). For all the electrochemical measurements, the working electrode was initially cathodically polarized at −1.2 V_{SCE} for 120 s to remove air-formed oxidation products and to improve the reproducibility. Then, the open circuit potential (OCP) was monitored for 10 h to indicate the existence of the necessary quasi-steady state of the system before initiating the EIS measurements. The stable OCP values after 10 h of exposure are presented in Table 2. The EIS data were recorded twice by stepping the frequency from 10,000 to 0.01 Hz in 10 steps/decade, and then immediately stepping the frequency back to 10,000 Hz with an excitation voltage of 10 mV. The potentiodynamic polarization (PDP) measurements were conducted after half an hour rest at the OCP at 30 ℃, scanning from −0.55 V_{SCE} (around −0.2 V lower than OCP) to the pitting potential (E_p) or the oxygen evolution potential at a sweep rate of 0.5 mV/s to determine the passive range of HDSS 2707 in the simulated solution. Based on the passive region obtained from the PDP curve, films were formed at potentials of −0.5 V_{SCE}, −0.2 V_{SCE}, −0 V_{SCE}, + 0.2 V_{SCE} and + 0.4 V_{SCE} and these potentials were selected to conduct potentiostatic polarization studies. Each potentiostatic polarization lasted for 5 h in order to stabilize the passivation of HDSS 2707 surface, and to achieve a steady-state of the electrochemical system before EIS measurements. Mott-Schottky (M-S) plots were measured by recording the imaginary component of the impedance at 1 kHz while stepping the potential in the positive direction every 16 s in increment of 50 mV from −0.4 V_{SCE} to +0.4 V_{SCE}. The capacitance and hence the barrier layer thickness were then calculated from the measured imaginary component of the impedance. This procedure was adopted to maintain the bl thickness and the point defect structure voltage independent during the M-S measurement, which brings the system into better compliance with M-S theory. Note that the bls generally dissolve very slowly (of the order of 10^{-2} to 10^{-4} nm/s) and, because the point defect diffusivity is very small (10^{-18} to 10^{-20} cm^2/s) the relaxation time for the defect structure is very long. In this way, the bl thickness and the defect structure are “frozen-in” during the M-S measurement at any formation voltage. All the

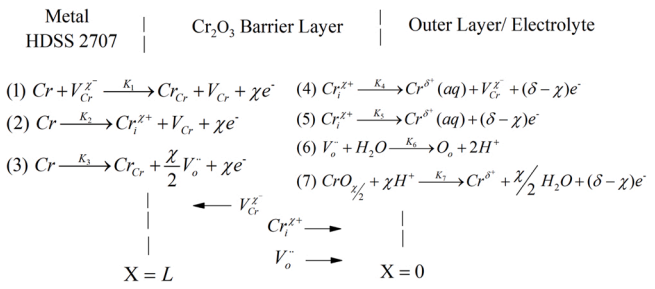

Fig. 1. Point defect interface reactions in the growth of anodic barrier oxide films according to the PDM. Cr is chromium atom in metal; $V_{cr}^{\chi-}$ is chromium vacancy in barrier layer; $Cr_{Cr}$is chromium cation in normal cation sublattice in barrier layer; V_{Cr} is vacancy of chromium atom in metal; $Cr_i^{\chi+}$ is chromium cation interstitial in barrier layer; $V_o^{\cdot\cdot}$ is oxygen vacancy in barrier layer; $Cr^{\delta+}$ (aqueous ions) is chromium cation in solution; O_o is oxide ion in anion sublattice in barrier layer; $CrO_{\chi/2}$ is stoichiometric barrier layer oxide; χ is oxidation states of chromium in barrier layer; δ is oxidation states of chromium in solution [8,41].

Table 3
Functional forms of the rate constants for reactions (1)–(7) and the exponential coefficients for these rate constants. $k_i = k_i^0 e^{a_i V} e^{b_i L_{ss}} e^{c_i pH}$ [8,41].

Reactions (1)–(3) $i = 1, 2, 3$	$k_i{}^0 = k_i{}^{00} e^{-\chi\alpha_i\gamma\varphi_{fs}^0}$; $a_i(V^{-1}) = \alpha_i(1-\alpha)\chi\chi$; $b_i(cm^{-1}) = -\chi\alpha_i\gamma\varepsilon$; $c_i = -\chi\alpha_i\gamma\beta$
Reaction (4)–(6) $i = 4, 5, 6$	$k_i{}^0 = k_i{}^{00} e^{-\delta\alpha_i\gamma\varphi_{fs}^0}$; $a_4(V^{-1}) = \alpha_4\alpha\gamma\delta$; $a_5(V^{-1}) = \alpha_5\alpha\gamma\delta$; $a_6(V^{-1}) = 2\alpha_6\alpha\gamma$; $b_i(cm^{-1}) = 0$; $c_4 = \alpha_4\beta\delta\gamma$; $c_5 = \alpha_5\beta\delta\gamma$; $c_6 = 2\alpha_6\beta\delta\gamma$
Reaction (7)	$k_7^0 = k_7{}^{00} e^{(\delta-\chi)\alpha_7\gamma\varphi_{fs}^0}$; $a_7(V^{-1}) = \alpha_7\alpha\gamma(\delta-\chi)$; $b_7(cm^{-1}) = 0$; $c_7 = \alpha_7\gamma\beta(\delta-\chi)$

Note：k_i is the rate constants for reaction i; k_i^0 is the standard rate constant; k_i^{00} is the base rate constant; a_i, b_i, c_i is the exponential coefficients; V is the applied external potential; L_{ss} is the barrier layer thickness; φ_{fs}^0 represents the standard potential of film/solution interface; α is the polarizability of the film/solution interface; α_i is the transfer coefficients; $\gamma = F/RT$, F is Faraday's constant; β is the effect of pH on the potential drop across the film/solution interface.

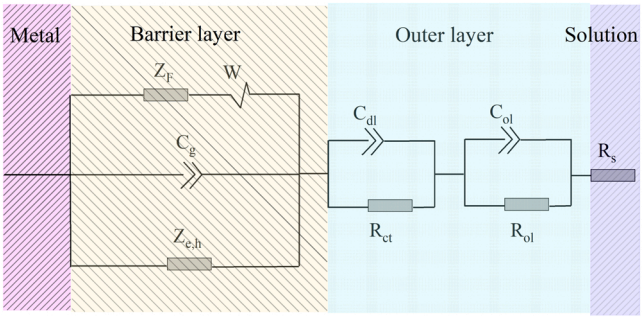

Fig. 2. Schematic of the equivalent electrical circuit for the whole electrochemical reaction system of HDSS 2707.

electrochemical measurements were carried out using a Gamry PC4 potentiostat.

3. Mixed potential model (MPM)

In this paper, for modeling the passive film formation on HDSS 2707, the mixed potential model (MPM) that was previously proposed by Macdonald et al., was used [35,36]. According to the PDM, the passive film on the steel surface is sensitive to the kinetics of the point defects, which are generated and annihilated at the metal/film (m/f) and film/solution (f/s) interfaces, as shown in Fig. 1 [37,38]. Therefore, the passive film is postulated to comprise a bilayer structure of a highly-defective barrier layer that grows into the metal, and a precipitated, porous layer that grows into the solution [8,39,40]. The barrier layer (bl) is based on the framework of Cr oxide and is protective for the metallic matrix because Cr oxide grows inwards via oxygen vacancy ($V_o^{\cdot\cdot}$) generation and transmission (cation vacancy transport is relevant only in the transpassive regime), see reaction 3 in Fig. 1. Interstitial cations of Fe, Ni, and Cr migrate through the barrier layer to be ejected at the bl/s interface and subsequently hydrolyze to form a porous outer layer (ol) by transporting via an interstitial mechanism. It is worth noting that while the model is written in terms of Cr, because that element forms the structure of the barrier layer, it is recognized that Fe and Ni are lumped together with Cr in producing interstitials. We simply do not have sufficient data to distinguish between them. That would require measurement of the component of the current that is attributable by each element. Thus, the rate constants for Reactions 2 and 5 in the PDM are best regarded as composite vales covering all metals in the alloy. The value of rate constant (k_i) for the i^{th} reaction in Fig. 1 is defined by the constant parameters including the standard rate constants (k_i^0), the base rate constants (k_i^{00}), transfer coefficients (α_i) and exponential coefficients (a_i, b_i, c_i), as shown in Table 3.

Based on the seven fundamental point defect reactions in Fig. 1, the bl thickness in the steady state can be expressed by Eq. (1), while the current under any set of conditions, including the non-steady state is in the form of Eq. (2) [29]:

$$L_{ss} = \left(\frac{1-\alpha}{\varepsilon}\right)V + \left(\frac{c_7 - c_3}{b_3}\right)pH + \frac{1}{\alpha_3\varepsilon\chi\gamma} ln\left[\frac{k_3^0}{k_7^0}\right] \tag{1}$$

and

$$i = F\left[\chi k_1 C_v^L + \chi k_2 + \chi k_3 + (\delta-\chi)k_4 + (\delta-\chi)k_5 C_i^0 + (\delta-\chi)k_7\right] \tag{2}$$

Under steady-state conditions, $k_1 C_v^L = k_4, k_2 = k_5 C_i^0, and k_3 = k_7$ and the steady-state current density becomes

$$i_{ss} = \delta F[k_2 + k_3 + k_4] \tag{3}$$

where α is the polarizability of the bl/solution (bl/s) interface, ε is the electric field strength within the bl, δ and χ are the oxidation states of the metal cation in the outer layer and in the barrier layer, respectively. The quantity [1-α]/ε is the anodizing constant. C_V^L is the concentration of cation vacancies at the m/bl interface, C_i^0 is the concentration of cation interstitials at the bl/ol interface, and k_i, a_i and b_i are parameters as defined in Table 3. By taking the derivative of i with respect to V, the faradaic impedance, Z_F, of the corrosion system can be derived as follows:

$$Z_F = Y_F{}^{-1} = \frac{\delta i}{\delta V} \tag{4}$$

$$Y_F = \frac{Y_F^0}{1 + R_{ol} Y_F^0} \tag{5}$$

where Y_F^0 is the faradaic admittance of the barrier layer, while Y_F is the faradaic admittance of the entire passive film including the outer layer. It is seen that $Y_F \to Y_F^0$ as $R_{ol} \to 0$, and $Y_F \to \frac{1}{R_{ol}}$ for $Y_F^0 \to \infty$ i.e., the interfacial impedance becomes controlled by the outer layer in the limit of an infinite outer layer specific resistance or an infinitely small barrier layer admittance.

As follows from Eq. (4) and reactions in Fig. 1, we have in the linear form [29]:

$$Y_F^0 = I_U + I_L \frac{\Delta L}{\Delta U} + I_V^L \frac{\Delta C_V^L}{\Delta U} + I_i^o \frac{\Delta C_i^0}{\Delta U} \tag{6}$$

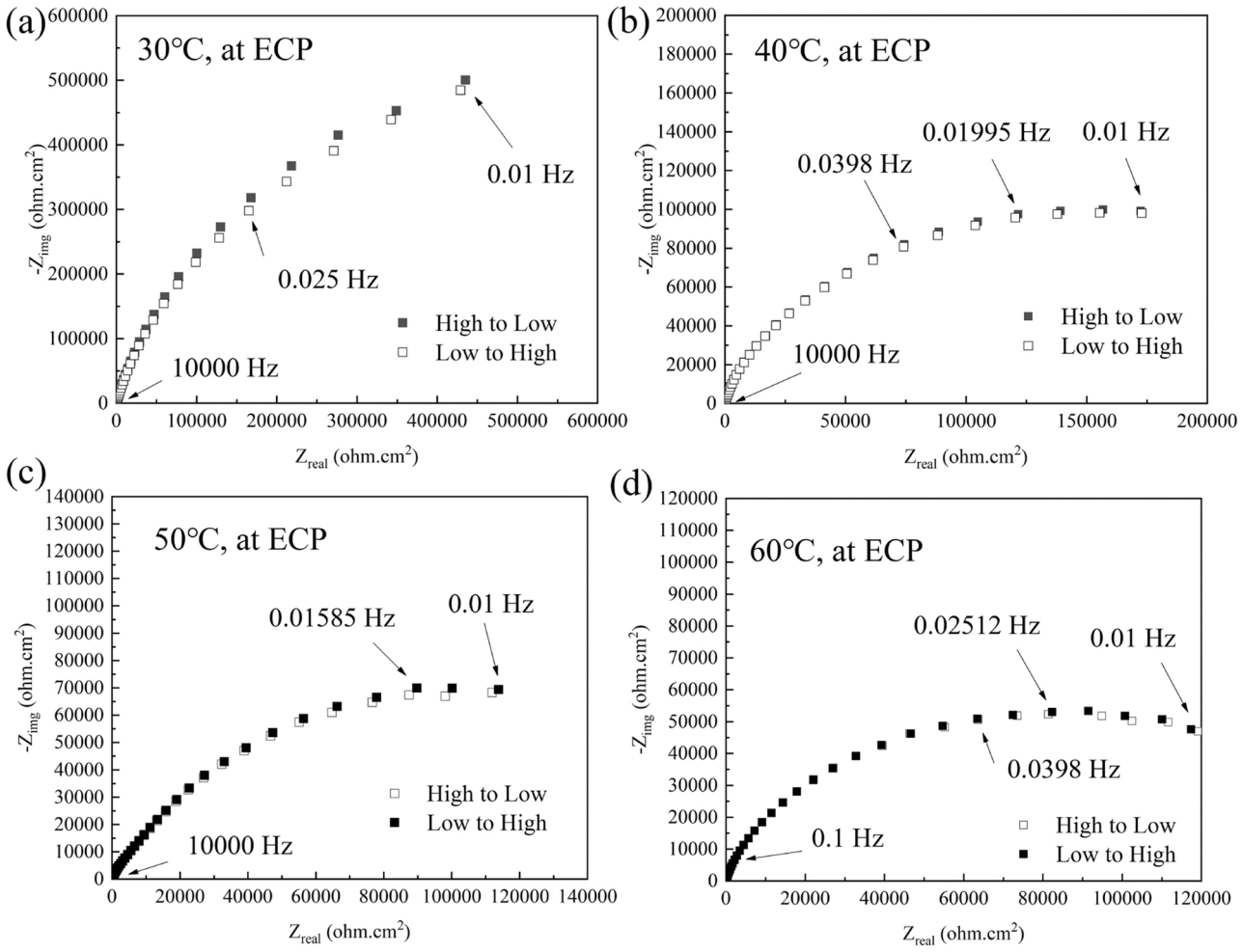

Fig. 3. Impedance plots of the measured EIS data in the Nyquist planes for two frequency step directions for passive film formed on HDSS 2707 at OCP in $(NH_4)_2CO_3$ solution containing 0.1 M Cl^- at different temperatures. The OCP values for each temperature are summarized in Table 2.

and

$$I_U = F\{\chi a_1 k_1 C_v^L + \chi k_2 a_2 + \chi k_3 a_3 + (\delta-\chi)k_4 a_4 + (\delta-\chi)k_5 a_5 C_i^0 + (\delta-\chi)k_7 a_7\} \quad (7)$$

$$I_L = -F(\chi b_1 k_1 C_e^L + \chi k_2 b_2 + \chi k_3 b_3) \quad (8)$$

$$I_V^L = F\chi k_1 \quad (9)$$

$$I_i^o = F(\delta-\chi)k_5 \quad (10)$$

$$\frac{\Delta L}{\Delta U} = \frac{\Omega(k_3 a_3 - k_7 a_7)}{j\omega + \Omega k_3 b_3} \quad (11)$$

where Ω is the molar volume of the barrier layer cation. If $\delta = \chi$, or the changes of the cation vacancy concentration can be neglected, which are a minority defect for a n-type semiconductor and we then have $Y_F^0 = I_U + I_L \frac{\Delta L}{\Delta U}$ [35]. In the MPM, the cathodic reaction, $O + ne^- \leftrightarrow R$ is described in terms of the Generalized Butler-Volmer equation as:

$$i_c = \frac{e^{\alpha_a \cdot \frac{F}{RT}(V-V_{eq})} - e^{-\alpha_c \cdot \frac{F}{RT}(V-V_{eq})}}{\frac{1}{i_0} + \frac{e^{\alpha_a \cdot \frac{F}{RT}(V-V_{eq})}}{i_{l,a}} - \frac{e^{-\alpha_c \cdot \frac{F}{RT}(V-V_{eq})}}{i_{l,c}}} \quad (12)$$

where α_a and α_c are the anodic and cathodic transfer coefficients for the reverse and forward directions of $O + ne^- \leftrightarrow R$, $i_{l,a}$ and $i_{l,c}$ are the corresponding mass-transfer limiting currents, i_0 is the exchange current density, and V_{eq} is the equilibrium potential (Table 2) [42].

The prevailing cathodic reaction for HDSS 2707 in the simulated buffer electrolytes ($(NH_4)_2CO_3$, pH = 13 ± 0.2) is the water reduction, and the cathodic limiting current ($i_{l,c}$) is infinite as water is the solvent [27]. Thus, setting $i_{l,c} = \infty$, the cathodic current density, i_c is expressed by [27,35]:

$$i_c = \frac{e^{\alpha_a \cdot \frac{F}{RT}(V-V_{eq})} - e^{-\alpha_c \cdot \frac{F}{RT}(V-V_{eq})}}{\frac{1}{i_0} + \frac{e^{\alpha_a \cdot \frac{F}{RT}(V-V_{eq})}}{i_{l,a}}} \quad (13)$$

Therefore, the currents for the partial hydrogen oxidation and the water reduction reactions of HER on the surface of the passive film can be written as:

$$i_{c,\ a} = \frac{e^{\alpha_a \frac{F}{RT}(V-V_{eq})}}{\frac{1}{i_0} + \frac{e^{\alpha_a \cdot \frac{F}{RT}(V-V_{eq})}}{i_{l,a}}} \quad (14)$$

$$i_{c,\ c} = \frac{-e^{-\alpha_c \frac{F}{RT}(V-V_{eq})}}{\frac{1}{i_0} + \frac{e^{\alpha_a \cdot \frac{F}{RT}(V-V_{eq})}}{i_{l,a}}} \quad (15)$$

In order to obtain the accurate partial current densities, a correction for i_0, related to the presence of the passive film on a metal surface due to the need for charge carriers (electrons and electron holes) to quantum mechanically tunnel (QMT) across the bl is used, as follows [42,43]:

$$i_0 = \hat{i}_0 exp(-\hat{\beta} L_{ss}) \quad (16)$$

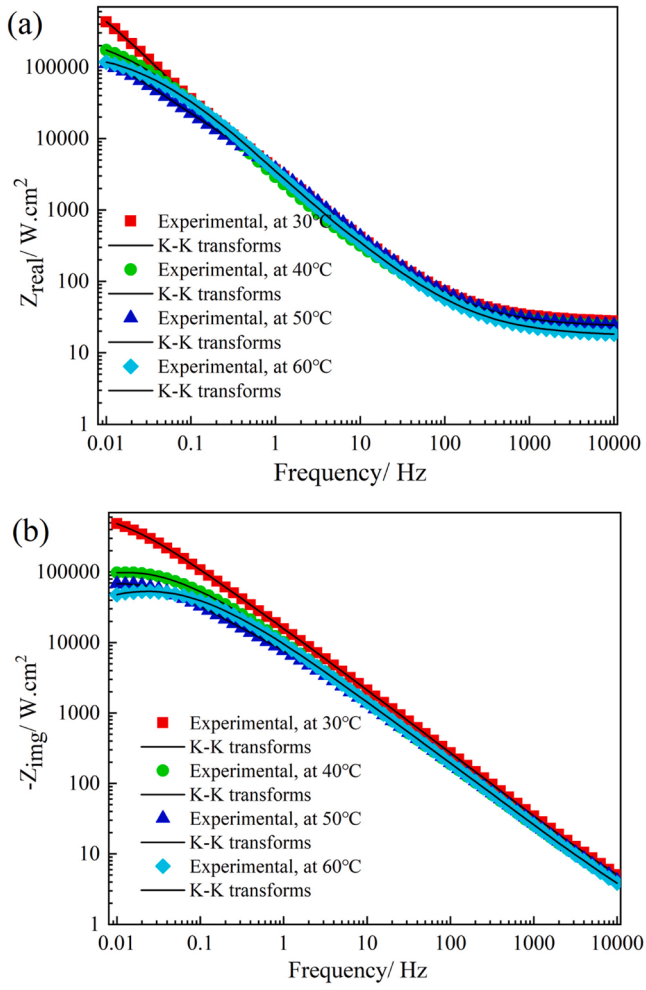

Fig. 4. Kramers-Kronig transforms of the real component (a) and imaginary component (b) of the impedance data of HDSS 2707 at OCP in $(NH_4)_2CO_3$ solution containing 0.1 M Cl^- at different temperatures. The OCP values for each temperature are summarized in Table 2.

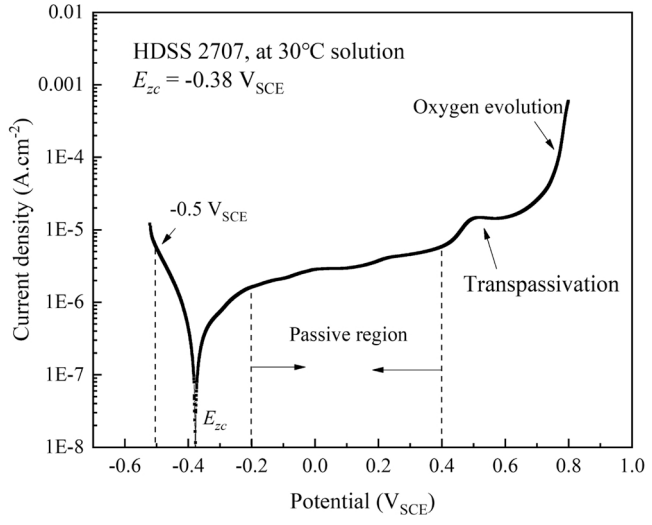

Fig. 5. Potentiodynamic polarization curve for HDSS 2707 in 0.2 M $(NH_4)_2CO_3$ + 0.1 M NaOH + 0.1 M NaCl, at the scan rate of 0.5 mV/s.

where $\widehat{\beta}$ is the tunneling constant, which is calculated by solving Schrodinger's equation for the appropriate barrier [44], $\widehat{i}_0$ is the exchange current density of the reaction on the bare metal ($L_{ss} = 0$). Substitution of Eq. (1) into Eq. (16) yields:

$$i_0 = \widehat{i}_0 exp\left[\frac{-\widehat{\beta}(1-\alpha)}{\varepsilon}V\right] exp(-\widehat{\beta}G) \tag{17}$$

where

$$G = \left(\frac{c_7 - c_3}{b_3}\right)pH + \frac{1}{\alpha_3 \varepsilon \chi \gamma} ln\left[\frac{k_3^0}{k_7^0}\right] \tag{18}$$

Substitution of Eq. (17) into Eq. (13) is yields:

$$i_c = \frac{e^{\alpha_a \frac{F}{RT}(V-V_{eq})} - e^{-\alpha_c \frac{F}{RT}(V-V_{eq})}}{\frac{1}{\widehat{i}_0 exp\left[\frac{-\widehat{\beta}(1-\alpha)}{\varepsilon}V\right] exp(-\widehat{\beta}G)} + \frac{e^{\alpha_a \frac{F}{RT}(V-V_{eq})}}{i_{l,c}}} \tag{19}$$

By taking the derivative of i_c with respect to V, the charge transfer impedance, Z_{ct}, is obtained. To avoid repetition, the details of the derivation of Z_{ct} can be found in Ref. [27,28].

$$Z_{ct} = (Y_{ct})^{-1} = \left(\frac{di_c}{dV}\right) \tag{20}$$

Thus, the total current density produced by the system is then the sum of i_{ss} and i_c,

$$i_{total} = i_{ss} + i_c \tag{21}$$

What needs illustration here is that when the applied potential is higher than the equilibrium potential of the HER (Table 2), $V > V_{eq}$, hydrogen oxidation dominates the cathodic reaction, so that i_c is positive. The above calculated faradic impedance (Eq. (4)) and the cathode impedance (Eq. (20)) can combine with other impedance components in the corrosion system to simulate the measured impedance of HDSS 2707 in $(NH_4)_2CO_3$ solution, and the Equivalent Electrical Circuit (EEC) is shown in Fig. 2. The total impedance of the corrosion system is written as:

$$Z = \left[\frac{1}{Z_F + Z_w} + \frac{1}{Z_{C_g}} + \frac{1}{Z_{e,h}}\right]^{-1} + \left(\frac{1}{Z_{C_{dl}}} + \frac{1}{R_{ct}}\right)^{-1} + \left[\frac{1}{Z_{C_{ol}}} + \frac{1}{R_{ol}}\right]^{-1} + R_s \tag{22}$$

where Z_W is the Warburg impedance associated with the transport of defects through the barrier layer in Fig. 1, and is expressed as:

$$Z_W = \frac{\sigma}{\sqrt{\omega}} - j\frac{\sigma}{\sqrt{\omega}} \tag{23}$$

where ω is the angular frequency and σ is the Warburg coefficient, Z_{C_g} is the impedance of the geometric capacitance of the dielectric barrier layer, and $Z_{e,h}$ is the electronic impedance due to the movement of the electrons and/or electronic holes. The quantity C_{dl} is the capacitance of the double layer, $Z_{C_{ol}}$ is the impedance arising from the geometric capacitance and the parallel specific resistance of the outer layer, R_{ol}, and R_s is specific resistance of the electrolyte (Ω cm^2). Note that the CPE is used to represent a distributed geometrical capacitance. Thus, on a polycrystalline surface, the barrier layer on each exposed grain face has a unique barrier layer thickness because of slight differences in the rate constants for Reactions (3) and (7) of the PDM. On any given face, the geometric capacitance is given by $C = \epsilon\epsilon_0 A/L$ where ϵ and ϵ_0 are the dielectric constant and the vacuum permittivity, respectively. A is the area, and L is the thickness of the barrier layer. With both A and L varying from grain face to grain face resulting in distribution in C, which appears to be effectively represented by a CPE.

In Fig. 2, it is illustrated that the passive film is divided into two layers with the barrier layer being a dense, point-defective, protective

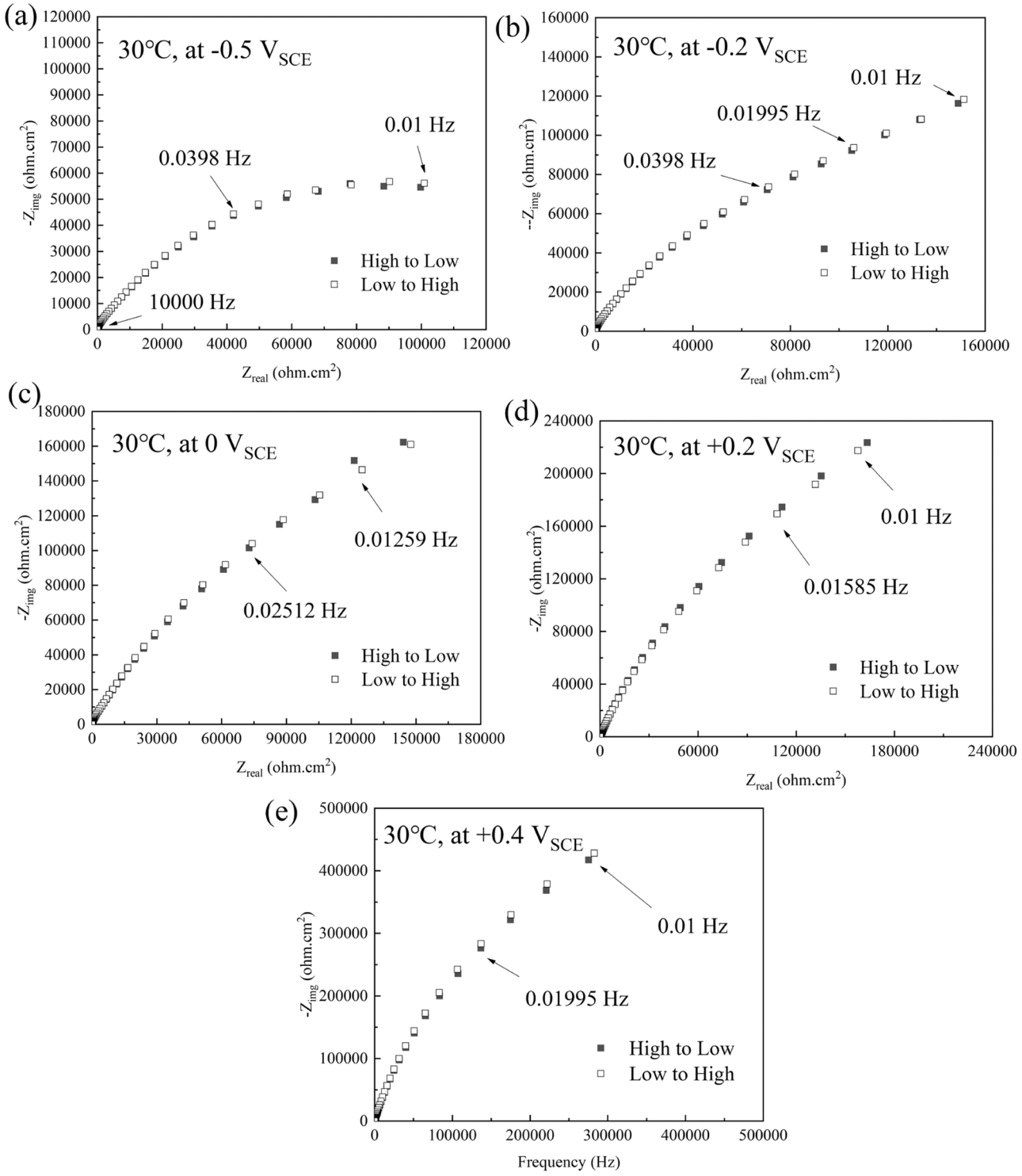

Fig. 6. Impedance plots of the measured EIS data in the Nyquist planes for two frequency step directions for passive film formed on HDSS 2707 in $(NH_4)_2CO_3$ solution containing 0.1 M Cl^- at 30 °C at different applied potentials.

layer on the metal surface, and thus is the main object of this study. Recognizing that, the potential that exists at the barrier layer can be expressed as [45]:

$$V_{bl} = V - iR_{ol} \tag{24}$$

where V is the applied voltage. Substitution of Eq. (2) into Eq. (24), the resistance of the barrier layer, R_{bl}, can be written as [26]:

$$R_{bl} = \frac{V - iR_{ol}}{F\left[\chi k_1 C_v^L + \chi k_2 + \chi k_3 + (\delta - \chi)k_4 + (\delta - \chi)k_5 C_i^0 + (\delta - \chi)k_7\right]} \tag{25}$$

and the steady-state barrier layer thickness in Eq. (1) can be modified to [26]:

$$L_{ss} = \left(\frac{1-\alpha}{\varepsilon}\right)\left(V - i_{ss}R_{ol}\right) + \left(\frac{c_7 - c_3}{b_3}\right)pH + \frac{1}{\alpha_3 \varepsilon \chi \gamma} ln\left[\frac{k_3^0}{k_7^0}\right] \tag{26}$$

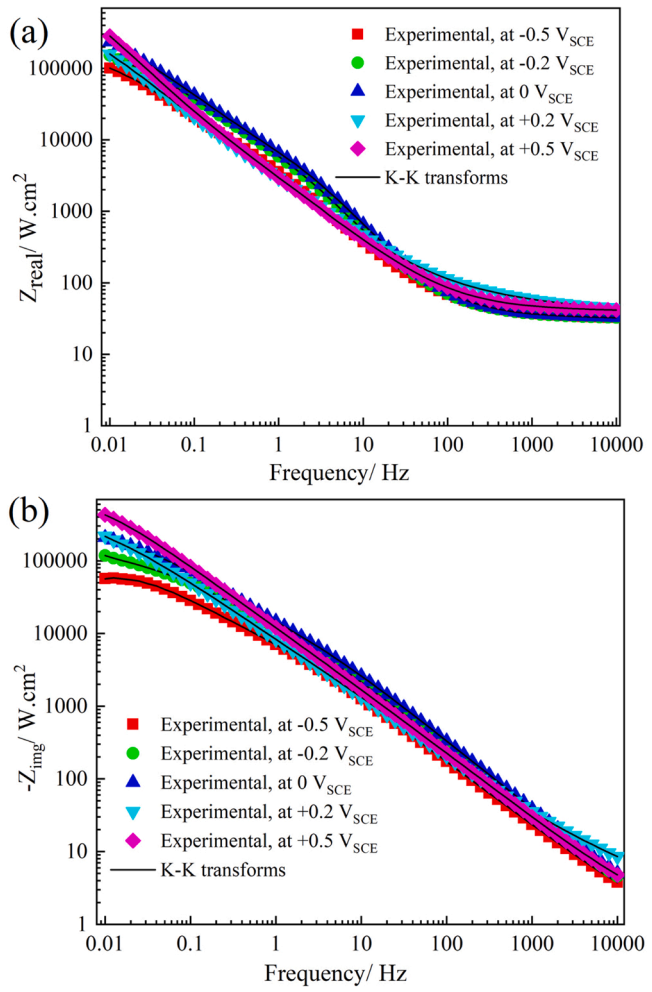

Fig. 7. Kramers-Kronig transforms of the real component (a) and imaginary component (b) of the impedance data of HDSS 2707 in $(NH_4)_2CO_3$ solution containing 0.1 M Cl^- at 30 ℃ at different applied potentials.

Table 4
The parameters that are held constant in optimization.

Parameters	Values
Polarizability of film/solution interface (α)	0.22 [16]
Dependence of $\phi_{f/s}$ on pH (β)	-0.0105 [16]
Kinetic order of Reaction 7 (n)	0.5 (Assumed)
Dielectric constant of the film ($\widehat{\varepsilon}$)	30 [55]
Tunneling constant ($\widehat{\beta}$)	4×10^7 (Assigned)
Oxidation state of cation in bl (χ)	+ 3 (Assigned)
Oxidation state of cation in ol/solution (δ)	+ 3 (Assigned)
Solution resistance (R_s)	25 Ω·cm^2 (Measured)
Molar volume of oxide per cation (Ω)	14.59 cm^3/mol (From density)

In the steady-state condition, the passive current density is also written as [45]:

$$i_{ss} = \frac{V}{R_{ol} + R_{bl}} \tag{27}$$

4. Results and discussion

4.1. Validity of impedance data

Since the stability of the electrochemical system during the EIS measurement is critical to obtain viable data for MPM optimization, the quality of the EIS data was checked both experimentally and theoretically, with latter being performed using the Kramers-Kronig transforms [30]. Fig. 3 show the EIS plots of HDSS 2707 measured in the high-to-low and low-to-high frequency stepping directions at the OCP (after OCP for 10 h) in Nyquist planes, respectively. The reliability of the data can be ascertained when the same responses were obtained at equivalent frequency in the two directions. Obviously, the recorded impedance data in the two different frequency stepping directions are coincident, implying the high stability of the passive film during the measurement, which means that the thickness and dissolved current density at the OCP are independent of time [35].

In order to further assure the quality of the EIS data, Kramers-Kronig (K-K) transforms were used to theoretically verify the linearly, stability, finiteness, and causality constraints of the measured system [46,47]. The K-K transforms calculate the real part from the imaginary part (or vice versa) of the response function (impedance or admittance) based on the interrelationship between analyticity and causality. Because of its purely mathematical origin from the definition of causality (via Cauchy's theorem), and since it does not assume any physical properties of the system, it is an ideal tool for examining data that originates from experiments under various circumstances that may result in violation of the constraints of Linear System Theory (LST). Fig. 4 exhibits the transformation results of the impedance data obtained at OCP, where the real and imaginary components calculated by K-K transformation are compared with experimental components. It is seen that a good agreement between the experimental and transformed data exists within the entire frequency range, demonstrating that the electrochemical system conforms to LST at the OCP, thereupon the passive film formed on the HDSS 2707 surface is at a steady state. Therefore, the corrosion kinetic parameters of HDSS 2707 obtained from MPM optimization and their correlation with the partial anodic reactions based on the PDM are discussed in the next section.

To determine the effect of the applied potential on the characteristic of the passive film, a typical polarization curve of HDSS 2707 in $(NH_4)_2CO_3$ solution containing Cl^- (pH = 13) measured with a potential sweep rate of 0.5 mV/s, at 30 ℃ was recorded and is presented in Fig. 5. It is seen that the passive current density is almost independent of applied voltage over a wide voltage range from −0.2 V$_{SCE}$ to 0.4 V$_{SCE}$, followed by a transpassive dissolution behavior at above 0.5 V$_{SCE}$ because of the oxidation of Cr (III) to Cr (VI) [48,49], with the final limit of the current being determined by the onset of oxygen evolution (0.8 V$_{SCE}$). No current transient and therefore no meta-stable pitting is observed over the entire potentiodynamic polarization measurement. The zero-current potential (E_{zc}) is about −0.38 V$_{SCE}$; therefore, a compilation of potentiostatic polarization experiments at different potentials of −0.5 V$_{SCE}$ (in cathode region), −0.2 V$_{SCE}$, 0 V$_{SCE}$, 0.2 V$_{SCE}$, and 0.4 V$_{SCE}$ were performed to study the passive state on HDSS 2707. The potentiostatic polarization at the above, selected five potentials each lasted for 5 hrs before commencing the EIS measurements in the resulting quasi-steady-state.

Similarly recorded EIS data in the Nyquist planes in the high-to-low and low-to-high frequency stepping directions for HDSS 2707 at different applied potentials are analyzed, as displayed in Fig. 6. It is clear that the EIS data measured in the two-directions show excellent coincidence, again implying that the electrochemical testing system is under steady state conditions. It is important to note that the potentiostatic polarization runs at the different potentials had to be held constant for 5 hrs to confirm the stability of the barrier layer, thereby assuring reproducibility of the data. Additionally, the quality of the EIS data were examined via the K-K transforms in Fig. 7. The calculated K-K transforms of the real and imaginary components of the EIS results obtained after 5 h of polarization from −0.5 V$_{SCE}$ to +0.4 V$_{SCE}$ in the simulated solutions are in good agreement with the experimental EIS spectra. This demonstrates that the electrochemical testing system satisfies the linearity, stability, and causality constraints of LST. Therefore, the electrochemical response of the system to a small-amplitude potential

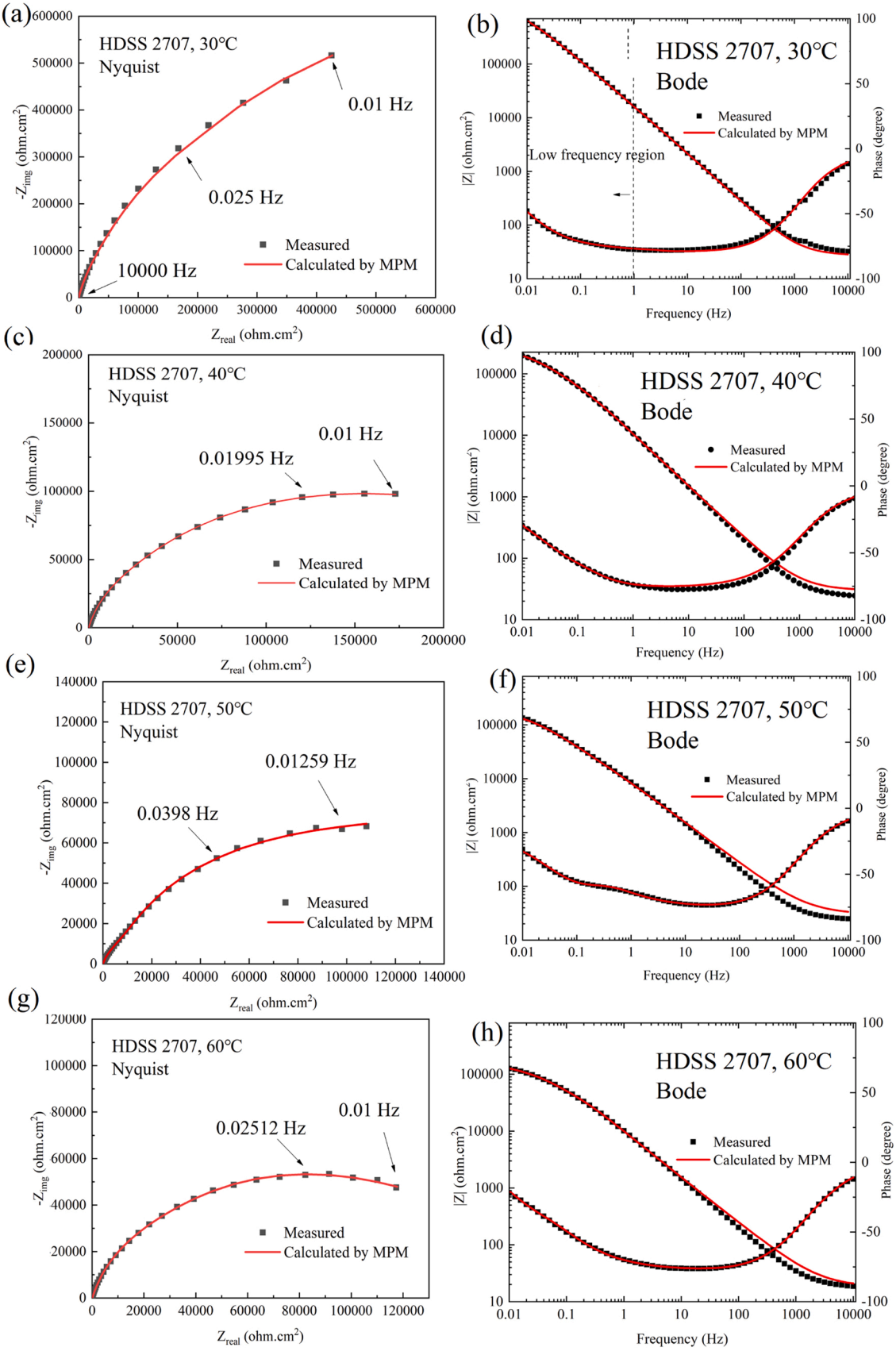

Fig. 8. Nyquist (a, c, e, g) and Bode (b, d, f, h) planes of HDSS 2707 at OCP at different temperatures in the $(NH_4)_2CO_3$ solutions containing Cl^-. Points represent experimental data; lines represent the simulated results by the MPM.

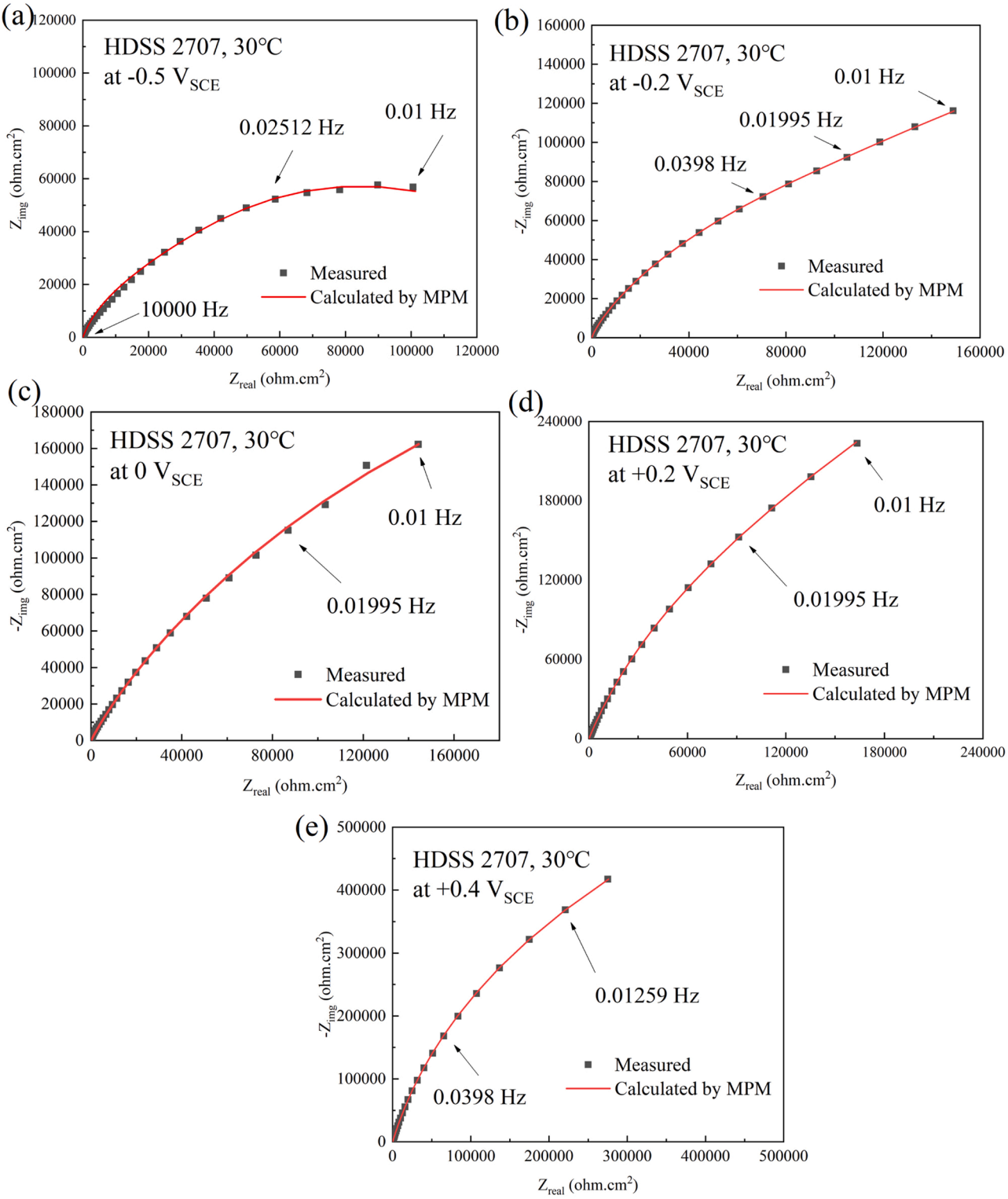

Fig. 9. Nyquist plots of HDSS 2707 in the $(NH_4)_2CO_3$ solutions containing Cl^- at different potentials at 30 ℃. Points represent experimental data; lines represent the simulated results calculated by the MPM.

perturbation can be described by linear response theory including linearized electrochemical models [50–52]. Again, the passive film formed on the HDSS 2707 surface after potentiostatic polarization lasted for 5 hrs was confirmed to reach the steady-state.

4.2. MPM optimization

Optimization of the MPM on the above qualified experimental EIS data was performed to extract values for the various model parameters and to ascertain the effects of temperature and applied potential on the passive films formed on HDSS 2707. As noted above, the MPM contains the PDM for the anodic dissolution of the passive metal, which describes

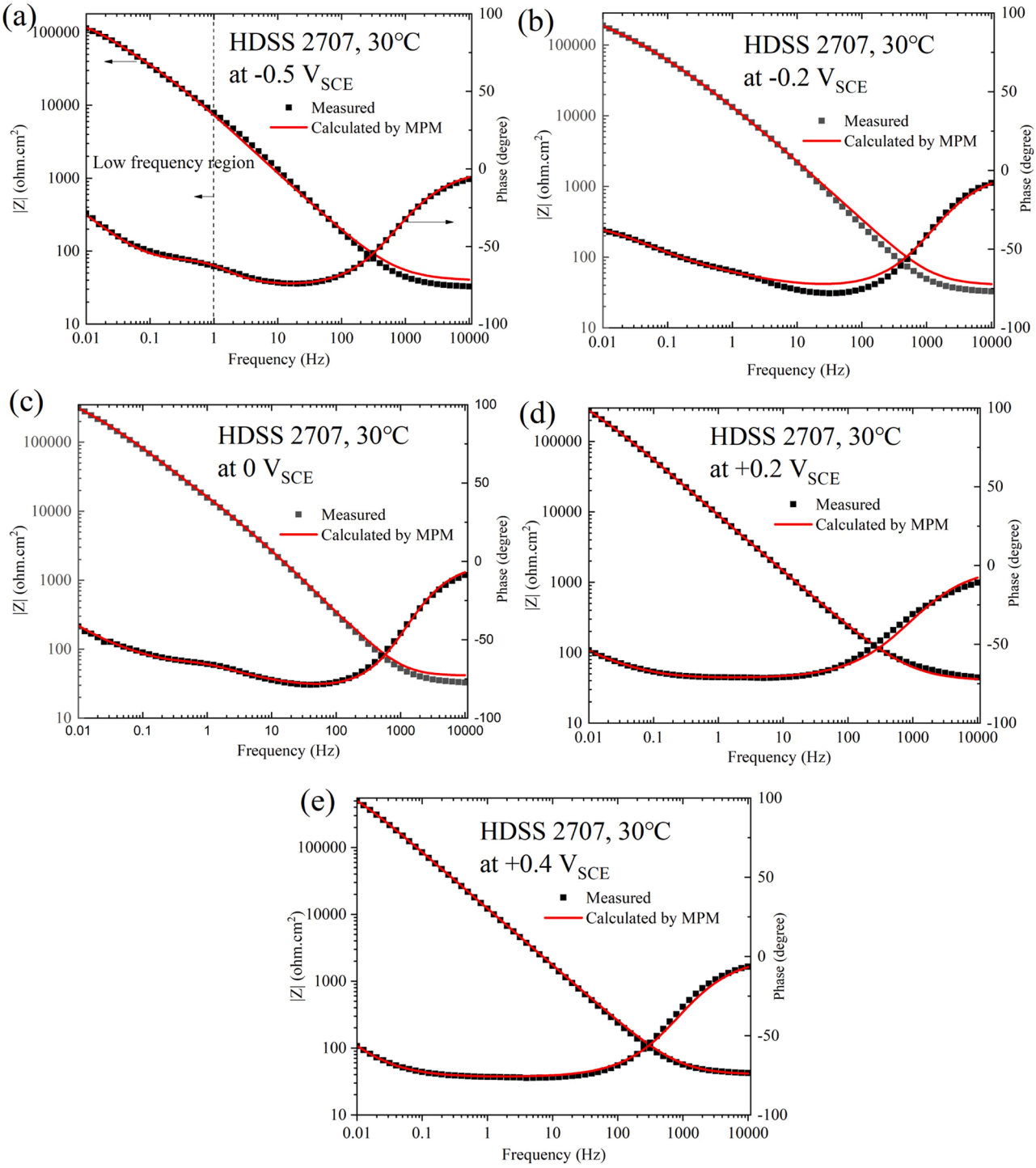

Fig. 10. Bode plots of HDSS 2707 in the $(NH_4)_2CO_3$ solutions containing Cl^- at different potentials at 30 ℃. Points represent experimental data; lines represent the simulated results by the MPM.

the stationary characteristics of the passive film, and the generalized Butler-Volmer equation (GBVE) for the cathodic reaction.

Optimization of the MPM on the EIS data is a process of obtaining a representation of a multivariate data set for an objective function [the impedance, Z, Eq. (22)] that describes a physical-electrochemical properties of the system [53,54]. The Igor Pro software (Version 6.37, WaveMetrics, Inc.) employing a genetic algorithm was used in this study for data fitting and parameters optimization. The resulting optimized parameters satisfy the following six requirements [29]: (a) All the parameter values are physically realistic and should exist within known bounds; (b) The calculated $Z'(\omega)$ and $Z''(\omega)$ should agree with the respective experimental results in both the Nyquist and Bode planes, and the tolerance value used in this work is 1×10^{-7}; (c) The EIS data satisfy the K-K transforms; (d) The values of the rate constants recovered by optimization must be consistent with the known electronic character of the bl as established by M-S analysis; (e) The predicted L_{ss} of bl and the i_{ss}, as a function of the appropriate independent variables (V and T) should agree within reasonable uncertainty with the experimental data; (f) The optimization process was carried out three times and the average parameters were reported. We should note that our optimization has

Table 5
Values of the parameters extracted from the optimization of the MPM on the experiment EIS data for passive film formed on HDSS 2707 in 0.2 M $(NH_4)_2CO_3$ + 0.1 M NaOH + 0.1 M NaCl at different temperatures.

Temperature/ ℃	30	40	50	60	Method
pH	13.19	12.87	12.69	12.52	Measured
$\chi/\ \delta/\alpha$	3/3/0.22	3/3/0.22	3/3/0.22	3/3/0.22	Assumed
α_2, α_3, α_7	0.42, 0.53, 0.48	0.58, 0.47, 0.49	0.52, 0.56, 0.52	0.48, 0.55, 0.47	1st stage
k_2^{00} (mol cm^{-2} s^{-1})	2.34×10^{-11}	5.11×10^{-11}	8.41×10^{-11}	4.28×10^{-10}	2nd stage
k_3^{00} (mol cm^{-2} s^{-1})	7.78×10^{-9}	1.03×10^{-8}	2.85×10^{-8}	5.62×10^{-8}	2nd stage
k_7^{00} (mol cm^{-2} s^{-1})	9.73×10^{-11}	3.76×10^{-10}	6.18×10^{-10}	9.78×10^{-10}	2nd stage
k_2 (mol cm^{-2} s^{-1})	5.67×10^{-13}	8.43×10^{-13}	4.17×10^{-12}	7.85×10^{-12}	2nd stage
k_5 (cm s^{-1})	2.71×10^{-10}	3.45×10^{-10}	8.54×10^{-10}	1.34×10^{-9}	2nd stage
k_3 (mol cm^{-2} s^{-1})	5.23×10^{-15}	7.86×10^{-15}	1.08×10^{-14}	3.28×10^{-14}	2nd stage
k_6 (cm s^{-1})	2.66×10^{-11}	3.21×10^{-11}	5.63×10^{-11}	8.31×10^{-11}	2nd stage
k_7 (mol cm^{-2} s^{-1})	9.73×10^{-11}	3.76×10^{-10}	6.18×10^{-10}	9.78×10^{-10}	2nd stage
σ	1622	2142	2241	2560	2nd stage
ε (*V*/cm)	2.00×10^{6}	1.60×10^{6}	1.30×10^{6}	1.00×10^{6}	2nd stage
L_{ss} (nm)	1.98	2.52	3.04	3.43	3rd stage
i_{ss} (A/cm^2)	8.13×10^{-8}	1.52×10^{-7}	4.74×10^{-7}	6.36×10^{-7}	3rd stage
i_c (A/cm^2)	-7.81×10^{-8}	-1.41×10^{-7}	-3.53×10^{-7}	-5.08×10^{-7}	3rd stage
$C_i^0 = k_2/k_5$ (mol cm^{-3})	2.12×10^{-3}	2.44×10^{-3}	4.88×10^{-3}	5.92×10^{-3}	3rd stage
$C_{V_0}^0 = \chi k_3/2k_6$ (mol cm^{-3})	2.83×10^{-4}	3.67×10^{-4}	2.88×10^{-3}	5.85×10^{-3}	3rd stage
R_{ct} (Ω cm^2)	5.39×10^{5}	4.26×10^{5}	3.09×10^{5}	1.24×10^{5}	3rd stage
R_{ol} (Ω cm^2)	9.20×10^{4}	7.31×10^{4}	6.45×10^{4}	3.51×10^{4}	3rd stage
CPE-Y_g (μF cm^{-2} s^{n-1})	3.82×10^{-6}	2.41×10^{-5}	4.71×10^{-6}	3.68×10^{-5}	3rd stage
CPE-Y_{ol} (μF cm^{-2} s^{n-1})	1.51×10^{-5}	1.86×10^{-5}	1.92×10^{-5}	1.83×10^{-5}	3rd stage
CPE-Y_{dl} (μF cm^{-2} s^{n-1})	1.87×10^{-4}	3.25×10^{-4}	5.95×10^{-4}	8.64×10^{-4}	3rd stage

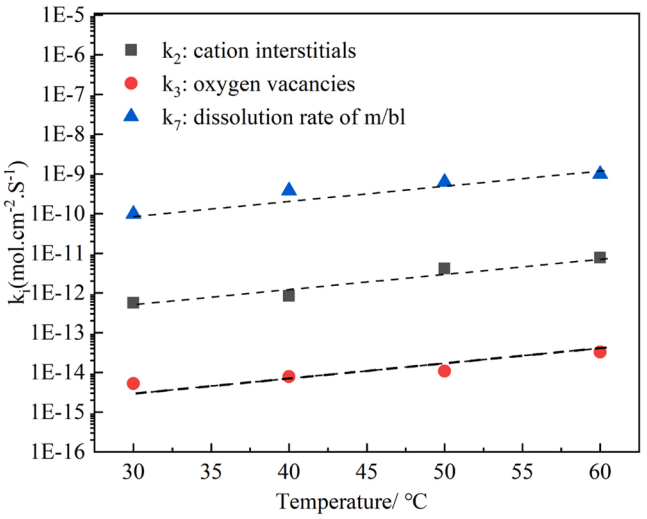

Fig. 11. The rate constant k_i as a function of temperature obtained by PDM on the EIS data at OCP.

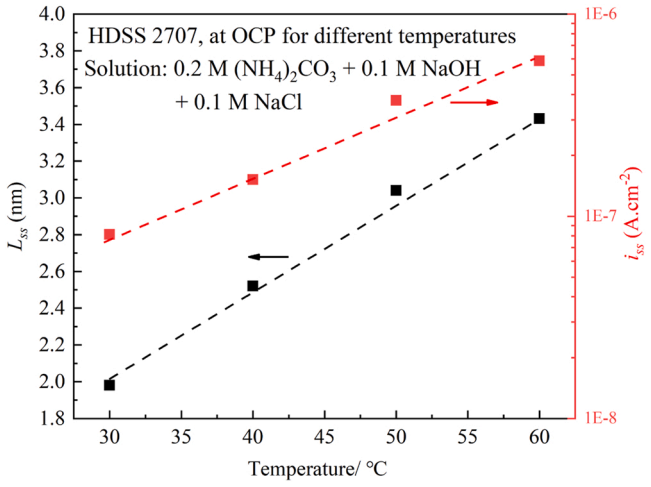

Fig. 12. The steady-state anodic current density and the thickness of the barrier layer on HDSS 2707 as a function of temperature at OCP in 0.2 M $(NH_4)_2CO_3$ + 0.1 M NaOH + 0.1 M NaCl.

been demonstrated to be reliable by calculating EIS spectra from the MPM using selected values for all parameters and then optimizing the MPM on the synthetic EIS data to successfully recover the assumed parameters from different sets of initial values for the unknowns.

Table 4 contains the parameter that are held constantly during the optimization based on our previous work for HDSS 2707 [16]. Fig. 8 displays the impedance data of HDSS 2707 at different temperatures at OCP, obtained from the optimization of MPM on experimental EIS data. Good agreement is observed between the simulated and measured results, indicating the rationality of the PDM. Similarly, Figs. 9 and 10 show the Nyquist and the Bode planes of the optimized impedance data of HDSS 2707 at different applied potentials at 30 ℃, respectively. The simulated results by MPM are coincident with the experimental measurements. What should be emphasized here is that the optimization results obtained from the low frequency regions are much more accurate than those obtained from the high frequency regions. This is important, because the rate constants have much greater impact on the impedance at low frequencies that do passive elements such as geometric capacitance, and we are primarily interested in defining the kinetic aspects of the passive film.

4.3. Effect of temperature on the passive film

Based on the above analysis, the parameters of the passive film formed on HDSS 2707 at OCP at different temperatures are extracted with minimized error (optimization) as listed in Table 5. It is observed that both the Warburg coefficient (σ) and the rate constants (k_i) increase with the increasing of temperature, while the charge transfer impedance (R_c), the resistance of the outer layer (R_{ol}), and the geometric capacitance (C_g) decrease. Based on Table 5, Fig. 11 shows that the reaction rates (k_2, k_3 and k_7) of the point defects increase with the temperature because the generation and annihilation of the interstitial defects are thermally activated. It is also found that, in all cases, k_2 is higher than k_3, manifesting that the cation interstitial (Cr_i^{3+}) rather than the oxygen

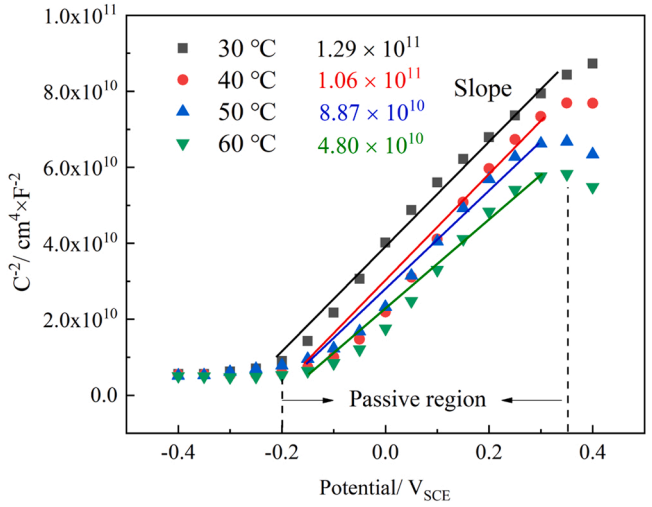

Fig. 13. Mott-Schottky plots of the passive film on HDSS 2707 at OCP at different temperatures.

Table 6
The effect of temperature on the steady-state anodic current density and corrosion rate of HDSS 2707 at OCP in the solution of 0.2 M $(NH_4)_2CO_3$ + 0.1 M NaOH + 0.1 M NaCl.

T/ ℃	I_{ss} /A.cm^{-2}	CR (μm/year)
30	8.13×10^{-8}	0.64
40	1.52×10^{-7}	1.19
50	4.74×10^{-7}	3.72
60	6.36×10^{-7}	5.52

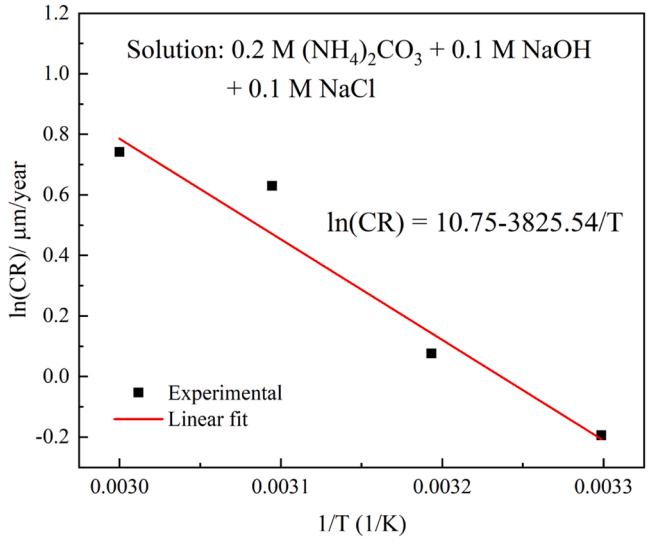

Fig. 14. Arrhenius linear plots of the logarithm of the steady-state anodic current density (i_{ss}) of HDSS 2707 in the solutions versus the reciprocal of temperature (1/T).

vacancy ($V_o^{\cdot\cdot}$) is the dominant point defect, and that the interstitial is responsible for the n-type semiconductor characteristic of the bl [24,26,56]. This is probably due to the larger radius of oxygen vacancy ($V_o^{\cdot\cdot}$) as compared to Cr, Fe and Ni interstitial, which requires a higher vacancy formation energy [34]. The parameter k_1 controls the annihilation of the minority defect, the cation vacancy at m/bl interface (Fig. 1), and the value is negligible when compared with k_2 and k_3 [26]. Thus, while cation vacancies are important is accounting for passivity breakdown, they are nevertheless a minority defect and exert little influence over the electronic character of the bl on HDSS 2707. Note that k_i^{00}, the base rate constant for each kinetic reaction, does not reveal the actual reaction rate, and it is k_i that directly reflects how fast the reactions proceed.

Fig. 12 displays the thickness (L_{ss}) of the barrier layer as a function of temperature, which is approximately 2 ~ 3.5 nm on HDSS 2707 surface in $(NH_4)_2CO_3$ solution, and increases with the increasing of temperature. Such variation for L_{ss} is associated with the increment of the anodizing constant [(1-α)/ε] (Eq. (1)) with temperature, which is the direct consequence of the decrement of the electric field strength ε (as revealed in Table 5), possibly ascribed to the thermal excitation of electron/electron hole pairs which in turn suppress the electric field strength [36]. As expected, it is apparent that both the electric field strength and the rate constants are temperature-dependent.

Additionally, the effects of temperature on the steady-state anodic current density of HDSS 2707, obtained from MPM optimization are shown in Fig. 12. It is clear that the anodic current density, i_{ss}, increases with increasing temperature. As mentioned above, the passive film is an n-type semiconductor, i.e., $(k_2 + k_3)$ " k_1 due to the cation vacancy being the minority point defect, and no change occurs in the oxidation state of the cation upon ejection from the barrier layer (δ = χ, in Table 4) within the passive region. Thus, the Eq. (2) can be simplified to:

$$i_{ss} = F[\chi k_2 + \chi k_3] \tag{28}$$

Evidently, the anodic current density is determined by k_2 and k_3, and increases with the increasing of the rate constants. To further confirm the above conclusions, M-S measurements were conducted, as shown in Fig. 13. The basic M-S equation for an n-type semiconductor is shown as follows:

$$C^{-2} = \frac{2}{eN_D\widehat{\varepsilon}\varepsilon_0}\left(V - V_{fb} - \frac{kT}{e}\right) \tag{29}$$

where C is the space charge capacitance, e is the elementary charge (1.6×10^{-19} C), ε_0 is the vacuum permittivity (8.85×10^{-14} F/cm), $\widehat{\varepsilon}$ is the dielectric constant of the passive film (assumed as 12 for the chromic barrier layer), V_{fb} is the flat band potential of the film, k is Boltzmann's constant (1.38×10^{-23} J/K), T is the Kelvin temperature (K), and N_D is the charge carrier density. It is clear that the slope of all the C^{-2} versus potential curves are positive, implying an n-type semiconductor characteristics of the barrier layer, which is in accordance with MPM prediction. The charge carrier density, N_D, of the passive film formed at different temperatures was calculated from the slope of the linear region (Fig. 15) based on Eq. (29). The value of fitted slopes of M-S plots at 30 ℃, 40 ℃, 50 ℃ and 60 ℃ are 1.29×10^{11}, 1.06×10^{11}, 8.87×10^{10}, and 4.80×10^{10}, respectively. The corresponding calculated N_D are 9.15×10^{19}, 1.11×10^{20}, 1.33×10^{20} and 2.45×10^{20} (cm^{-3}), illustrating a significant increase in the concentrations of the dominant point defects (Cr_i^{3+} and $V_o^{\cdot\cdot}$) with increasing temperature. Based on the MPM optimization of the rate constant k_i (in Table 5), the concentrations of the cation interstitials $C_i^0 = k_2/k_5$, and of the oxygen vacancies $C_{V_0}^0 = \chi k_3/2k_6$ inside the barrier layer are obtained. Hence, the charge carrier density, N_D is equal to the sum of the two defects indicated by PDM. Thus, the calculated defect density is $(C_i^0 \times NA + C_{V_0}^0 \times NA)$ around ~ 10^{21} cm^{-3}, where NA is Avogadro constant (6.02×10^{23}). Note that the optimization of donor density of MPM represents the theoretically maximum defect density, which should be higher than that M-S measurement because the concentration of the metal interstitial within the barrier layer is limited.

Based on the PDM, and recognizing that considerable amounts of iron and nickel also exist in the bl on stainless steel, the principal point defect is the metal interstitial (i.e., Cr_i^{3+}, Fe_i^{3+}, and Ni_i^{2+}) because the rate of formation of M_i^{n+} is much greater than that of $V_o^{\cdot\cdot}$. The interstitials migrate from the m/bl interface towards the bl/s interface, driven by the existing electric field (ε) inside the barrier layer [37]. For all

Table 7
Values of the parameters extracted from the optimization of the MPM on the experiment EIS data for passive film formed on HDSS 2707 in solution containing 0.2 M $(NH_4)_2CO_3$ + 0.1 M NaOH + 0.1 M NaCl at 30 ℃ at different potentials.

Potential/V_{SCE}	-0.5	-0.2	0	+0.2	+ 0.4	Method
α	0.21	0.21	0.21	0.21	0.21	Measured
χ / δ	3/3	3/3	3/3	3/3	3/3	Assumed
α_2, α_3, α_7	0.32, 0.58, 0.28	0.46, 0.63, 0.22	0.43, 0.58, 0.22	0.56, 0.57, 0.20	0.43, 0.51, 0.23	1st stage
n	0.54	0.53	0.52	0.51	0.53	1st stage
σ	2415	2386	2126	2434	2673	2nd stage
k_2^{00} (mol cm^{-2} s^{-1})	3.50×10^{-10}	5.49×10^{-10}	4.33×10^{-10}	3.77×10^{-10}	4.29×10^{-10}	2nd stage
k_3^{00} (mol cm^{-2} s^{-1})	6.05×10^{-11}	5.62×10^{-11}	5.90×10^{-11}	5.93×10^{-11}	6.37×10^{-11}	2nd stage
k_7^{00} (mol cm^{-2} s^{-1})	2.32×10^{-10}	2.04×10^{-10}	1.81×10^{-10}	1.94×10^{-10}	1.89×10^{-10}	2nd stage
k_2 (mol cm^{-2} s^{-1})	3.88×10^{-12}	3.37×10^{-12}	4.31×10^{-12}	3.70×10^{-12}	3.72×10^{-12}	2nd stage
k_3 (mol cm^{-2} s^{-1})	3.13×10^{-14}	2.43×10^{-14}	2.87×10^{-14}	2.93×10^{-14}	2.64×10^{-14}	2nd stage
k_7 (mol cm^{-2} s^{-1})	2.32×10^{-10}	2.04×10^{-10}	1.81×10^{-10}	1.94×10^{-10}	1.89×10^{-10}	2nd stage
α_c	0.20	0.19	0.18	0.19	0.19	3rd stage
L_{ss} (nm)	1.42	2.36	2.90	3.42	4.08	3rd stage
i_{ss} (A/cm^2)	8.42×10^{-8}	2.90×10^{-7}	3.07×10^{-7}	2.92×10^{-7}	3.03×10^{-7}	3rd stage
i_c (A/cm^2)	2.30×10^{-7}	5.16×10^{-7}	9.20×10^{-7}	1.23×10^{-6}	2.38×10^{-6}	3rd stage
$i_{c,a}$ (A/cm^2)	2.95×10^{-7}	5.32×10^{-7}	9.19×10^{-7}	1.24×10^{-6}	2.38×10^{-6}	3rd stage
$i_{c,c}$ (A/cm^2)	-6.47×10^{-8}	-1.67×10^{-8}	-3.27×10^{-9}	-6.49×10^{-10}	-1.36×10^{-10}	3rd stage
$\widehat{i_0}$(A/cm^2)	3.01×10^{-7}	3.58×10^{-7}	3.17×10^{-7}	2.84×10^{-7}	3.61×10^{-7}	3rd stage
R_{ct} (Ω cm^2)	9.43×10^{4}	3.55×10^{5}	6.90×10^{5}	9.75×10^{5}	1.49×10^{6}	3rd stage
R_{ol} (Ω cm^2)	1.85×10^{4}	1.68×10^{4}	1.50×10^{4}	9.80×10^{3}	6.78×10^{3}	3rd stage
CPE-Y_g (μF cm^{-2} s^{n-1})	4.16×10^{-6}	5.04×10^{-5}	1.10×10^{-5}	1.51×10^{-5}	2.09×10^{-5}	3rd stage
CPE-Y_{ol} (μF cm^{-2} s^{n-1})	5.41×10^{-6}	2.05×10^{-5}	7.43×10^{-6}	1.28×10^{-5}	2.47×10^{-5}	3rd stage
CPE-Y_{dl} (μF cm^{-2} s^{n-1})	3.40×10^{-5}	2.55×10^{-5}	2.12×10^{-5}	2.00×10^{-5}	1.46×10^{-5}	3rd stage

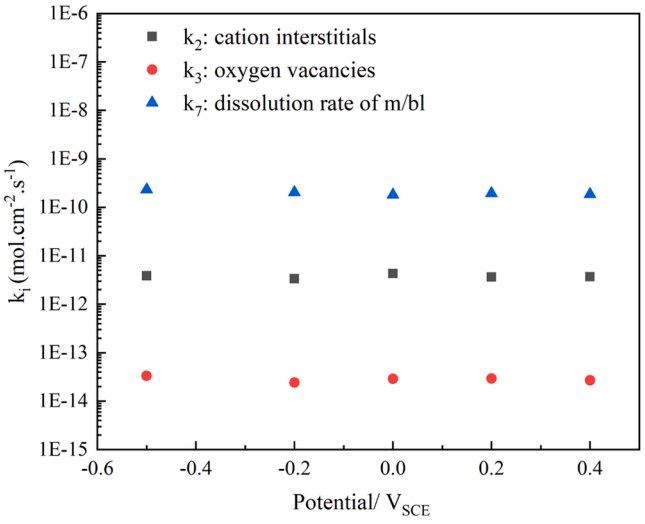

Fig. 15. The rate constant k_i as a function of potential obtained by MPM calculation on the measured EIS data at 30 ℃.

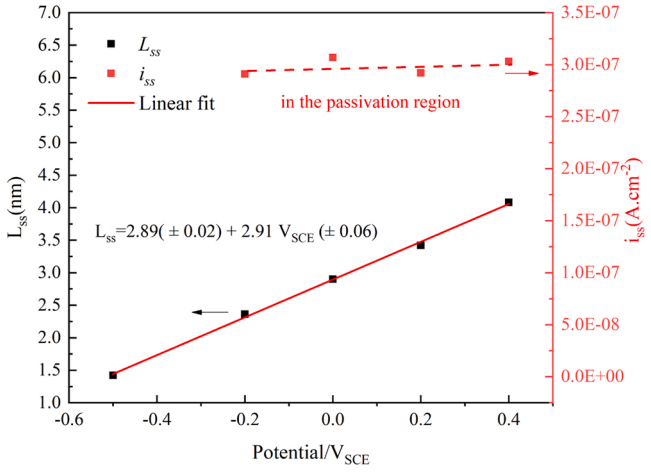

Fig. 16. The steady-state anodic current density and the thickness of the barrier layer on HDSS 2707 as a function of potential at 30 ℃ in the solution of 0.2 M $(NH_4)_2CO_3$ + 0.1 M NaOH + 0.1 M NaCl.

temperatures, $k_2 > k_3$ (Fig. 11), so that the dominant point defect is referred to as Cr_i^{3+} even though it is recognized that considerable substitution of Fe and Ni may exist in the bl, as is found to be the case for many other, if not all, chromium-containing alloys [28,49]. Therefore, the diffusivity (D) of the interstitial defect within the barrier layer can be estimated from the expression [57]:

$$D = 2\sigma^2(1-\alpha)^2 i_{ss}{}^2/\varepsilon^2 \tag{30}$$

where σ, α, i_{ss} and ε are listed in Tables 4 and 5. The calculated values of D of at 30 ℃, 40 ℃, 50 ℃ and 60 ℃ are 5.29×10^{-21} cm^2/s, 5.34×10^{-20} cm^2/s, 8.12×10^{-19} cm^2/s and 3.22×10^{-18} cm^2/s, respectively, which are in keeping with the findings in our previous research on HDSS 2707 [16]. Thus, the relaxation time of the defects, for example at 30 ℃, is $L_{ss}^2/D = (1.98 \times 10^{-7})^2 / 5.29 \times 10^{-21} = 7.41 \times 10^6$ s. The time between capacitance measurements (16 s) is much smaller than the relaxation time, and hence the defect concentration established in the barrier layer at the OCP is "frozen in" during M-S analysis, thereby fulfilling the important assumptions underlying M-S theory, as noted above.

By applying Faraday's law to the optimized net anodic current density (i_{ss}), the general corrosion rate (CR) of HDSS 2707 at different temperatures is calculated below:

$$CR = \frac{i_{ss} tM}{nF\rho} \tag{31}$$

where F is Faraday constant (96,485 C/mol); n is the number of equivalents exchanged, here assumed to be 3; M is the atomic weight of iron (56.5 g/mol); i_{ss} is the anodic current density; and ρ is the density of the steel (7.98 g/cm^3). The CR values are listed in Table 6. It is found that the value of CR of HDSS 2707 increases with the increasing temperature. The linear Arrhenius plot of the CR of HDSS 2707 versus the reciprocal of temperature (1/T) is shown in Fig. 14. By linear fitting, the relationship between the logarithm of the CR and the temperature is expressed as follows:

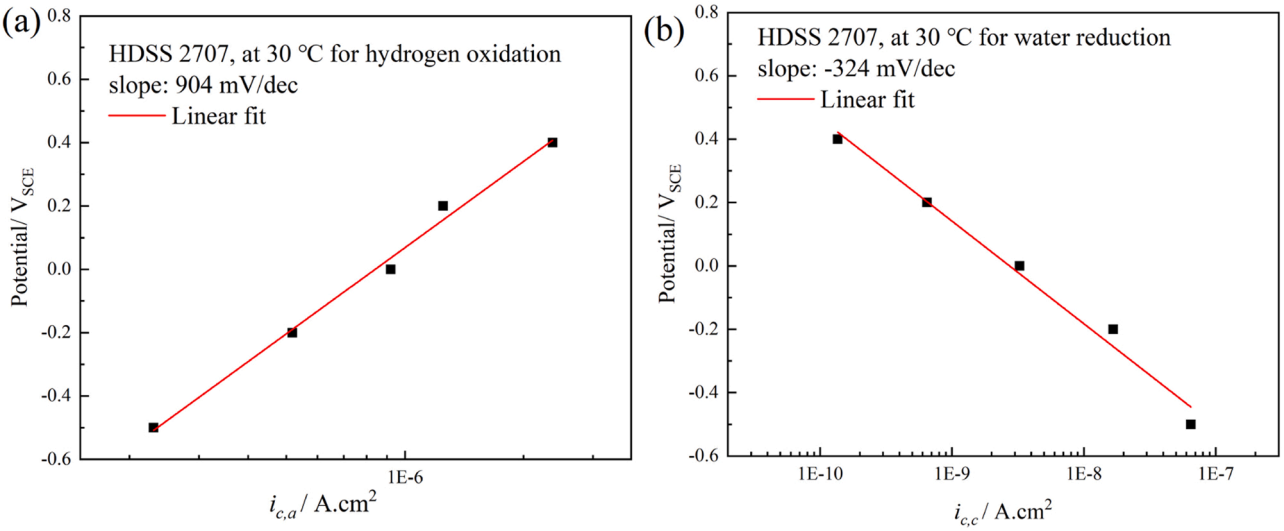

Fig. 17. Tafel plot for HER, (a) hydrogen oxidation and (b) water reduction, on passive HDSS 2707 based on the optimization of the MPM from Table 7.

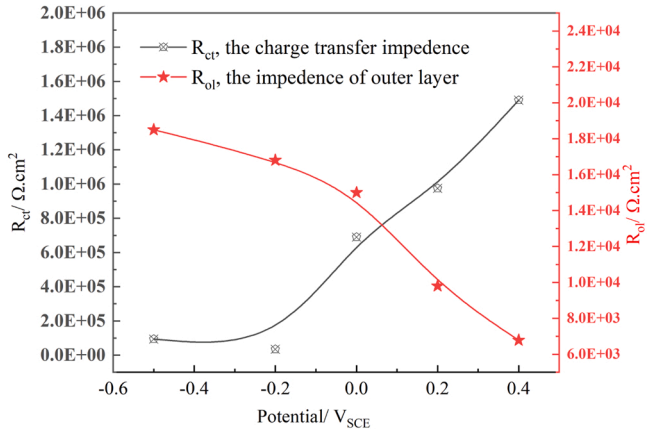

Fig. 18. The R_{ct} and R_{ol} values of the passive film formed on HDSS 2707 surface in the solution of 0.2 M $(NH_4)_2CO_3$ + 0.1 M NaOH + 0.1 M NaCl at 30 ℃ from optimization of the MPM.

$$ln(CR) = 10.75 - 3825.54/T \tag{32}$$

The decrease in the corrosion resistance of the specimen, corresponding to the increase in the *CR* with increasing temperature indicates that the defect density within the passive film plays a more important role than the film thickness in determining the corrosion resistance of HDSS 2707 in $(NH_4)_2CO_3$ solution.

From Table 5, we can see that the absolute values of i_{ss} (positive) and i_c (negative) are nearly equal, corresponding to the charge conservation condition, corresponding to the fact that the measured net current density at OCP is always zero (Eq. (19)).

4.4. Effect of applied potential on the passive film

Similarly, the parameters of the passive film formed on HDSS 2707 surface at different applied potentials at 30 ℃ based on MPM optimization are extracted with minimized error (optimization) as listed in Table 7. Fig. 15 shows the optimization values of the rate constant (k_i) as a function of the film formation potential, based on Table 7. It is observed that all the rate constants (k_2, k_3 and k_7) are essentially independent of the applied potential. According to the PDM, the rate constant for the generation and annihilation of the point defects at the interfaces in the steady-state can be written as $k_i = k_i^0 e^{a_i V} e^{b_i L_{ss}} e^{c_i pH}$, where a_i (V^{-1}), b_i (cm^{-1}) and c_i are defined in Table 3 in terms of fundamental quantities. From these definitions, together with Eq. (1), we find that $a_i V + b_i L_{ss} = -G$ (Eq. (18)) is a constant, thereby rendering the rate constant of k_2 and k_3 potential independent. In the case of Reaction (7) in Fig. 1, the rate constant k_7 is also potential independent since $\delta = \chi$ (Table 4), resulting in a_7 and c_7 are zero in Table 3.

Fig. 16 shows that the anodic current density, i_{ss}, is also independent to the applied potential in the passive region, because i_{ss} is determined by k_2 and k_3 (Eq. (28)), which is a constant at the steady state. On the other hand, on the basis of the PDM, by taking the derivative of i_{ss} with respect to V, the steady state current density is related to the applied potential by [24]:

$$\left(\frac{\partial \ln i_{ss}}{\partial V}\right)_{pH, C_{Cr}^{\delta+}} = k\alpha_7\left(\delta - \chi\right)\gamma \tag{33}$$

where k is a constant, $\gamma = F/RT$. For which $\delta = \chi$, the passive current density is calculated to be independent to the applied potential, implying n-type semiconductor properties of the passive film as predicted by the PDM [36,58–60], which is in agreement with M-S measurements (Fig. 13). From the optimization results, the average anodic current density at 30 ℃ is 0.31 μA/cm^2. Thus, the *CR* of HDSS 2707 in $(NH_4)_2CO_3$ solution at 30 ℃ is calculated (Eq. (31)) to be 2.36 μm/year.

The partial cathodic current density, i_c listed in Table 7, increases with the increasing of applied potential, where $i_c = i_{c,a} + i_{c,c}$ (Eqs. (14) and (15)). Since applied potential is greater than the equilibrium potential of the HER (V_{eq}, in Table 2), the hydrogen oxidation is the dominant reaction in $(NH_4)_2CO_3$ solution purged with ultrahigh purity N_2 + 4% H_2, and the trend of i_c is in keeping with $i_{c,a}$. It is worth noting that the passive current density measured by polarization curve in Fig. 5 is higher than ($i_{ss} + i_c$), because under potentiodynamic polarization conditions the surface is not at a steady state, and the faster the scan rate, the higher the passive current density [61].

The Tafel constant for HER between the passive film surface (i.e. b_a and b_c) and the film-free surface (i.e. $\hat{b}_a$ and $\hat{b}_c$) satisfy the following relationships [42]:

$$\frac{2.303}{\hat{b}_a} = \frac{2.303}{b_a} + \frac{\hat{\beta}(1-\alpha)}{\varepsilon} \tag{34}$$

$$\frac{2.303}{\hat{b}_c} = \frac{2.303}{b_c} - \frac{\hat{\beta}(1-\alpha)}{\varepsilon} \tag{35}$$

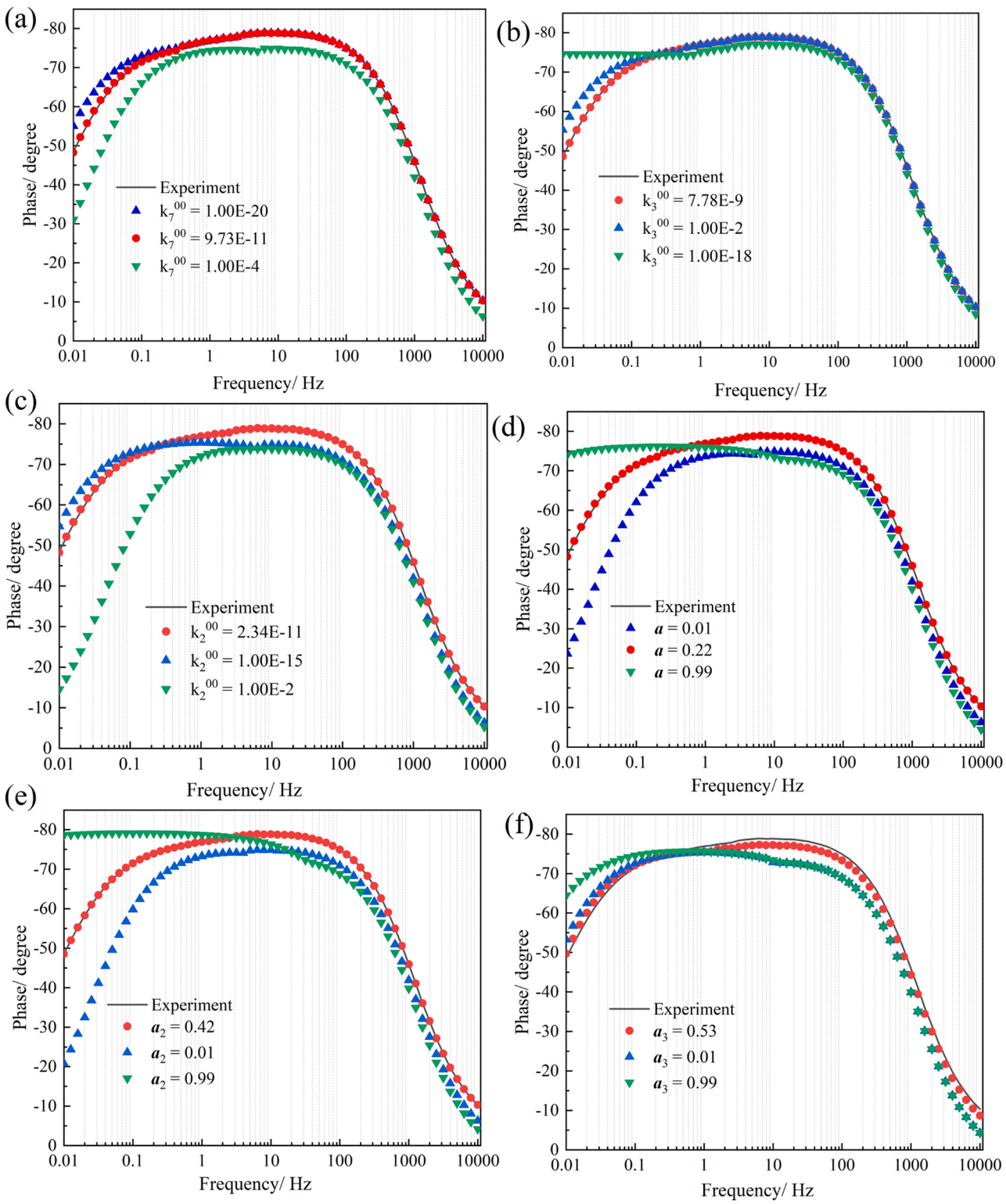

Fig. 19. Sensitivity analysis for the effect of the model parameters on calculated impedance. The default values for other parameters are given in Table 5.

where $b_a = \frac{2.303RT}{\alpha_a F}$ and $b_c = \frac{2.303RT}{\alpha_c F}$. As shown in Fig. 17, the Tafel slopes for the current density of hydrogen oxidation ($i_{c,a}$) and of water reduction ($i_{c,c}$) for the HER on the surface of the passive film are $b_a = 904$ mV/dec, and $b_c = -324$ mV/dec, respective. Based on the Eqs. (34) and (35), the $\widehat{b}_a$ and $\widehat{b}_c$ for the hydrogen evolution on the film-free HDSS 2707 surface are calculated to be 127 mV/dec and 101 mV/dec, where α and $\widehat{\beta}$ are listed in Table 4, and ε is 2×10^6 at 30 ℃. This demonstrates that the quantum mechanical correction (Eq. (16)) effectively remove the impact of the barrier layer on the kinetic of the HER, which is in consistent with the anodic and cathodic Tafel constants on the bare metal surface reasonably approximate those for the Heyrovsky mechanism on a noble metal like platinum [42].

The steady state thickness (L_{ss}) of the barrier layer calculated from Eq. (24), based on the extracted parameters from MPM is shown in Fig. 16. It is seen that L_{ss} increases linearly with the applied potential,

which is in accordance with our previous predictions [34,35]. The coefficient $\partial L_{ss}/\partial V = 2.91$ nm/V in Fig. 16, is higher than that of (2.36 nm/V) carbon steel in the SCPS solution (pH = 13.5) [62], suggesting that the passive film formed on HDSS 2707 is more dependent upon the electric field strength. Based on Eq. (30), as expected, the diffusivity, D, of the point defects at 30 ℃ at different applied potentials is constant, as well as is the transfer coefficient for the cathodic reaction, α_c, which is calculated to be 0.19 (Table 7), because both of them are materials properties.

Fig. 18 exhibits that the charge transfer resistance, R_{ct}, increases with the applied potentials as a result of the increasing of the barrier layer thickness (L_{ss}, in Fig. 16), while the outer layer resistance, R_{ol} decreases in values. From Eq. (24), it is seen that the current density times the outer layer resistance, $[i_{ss} \times R_{ol}]$ decreases with the applied potential in the passive region, thus giving rise to an increasing potential (V_{bl}) at the bl, thereby leading to the thickening of bl (Eq. (26)), as shown in Fig. 16.

4.5. Sensitivity studies

The importance of the kinetic parameters in controlling the impedance of the interface and hence the corrosion rate is illustrated in Fig. 19 (a)–(f). The changes in k_7^{00}, k_3^{00}, k_2^{00}, α, α_2, and α_3, respectively, are indicate in the figures and the values for other parameters are the default values given in Table 5. The EIS spectra calculated using the optimized parameter values correspond to the red points in all figures. Note that no variation in α_7 is includes because $\chi = \delta$ renders k_7 potential-independent, regardless of the value of α_7. The kinetic parameters are found to have their greatest effect on the phase angle at frequencies below 1000 Hz and to become increasingly impactful as the frequency is lowed. This emphasizes the need to obtain accurate EIS data to as low a frequency as possible and it also illustrates the impact that the point defect structure has on the interfacial properties of a passive substrate.

5. Summary and conclusions

In this paper, the formation kinetics of the passive layer on HDSS 2707 in $(NH_4)_2CO_3$ solution containing Cl^- at different temperatures and applied potentials were investigated. The optimization of the impedance model based on the mixed potential model (MPM) on the experimental EIS data has resulted in determination of the nature of the passive state of HDSS 2707. The main conclusions are summarized as follows:

1. From both experimental measurements and Kramers-Kronig transforms, the electrochemical system was verified to reach a quasi-steady state after the measurements of the initial 10 h open circuit potential and the later 5 h potentiostatic polarization. According to the MPM analysis based on the quasi-steady status of system, the thickness and dissolved current density of the passive film formed on HDSS 2707 surface are independent of time.
2. The MPM combining the point defect model (PDM) to describe the partial anodic reactions of the metal dissolution, and the generalized Butler-Volmer equation (GBVE) to describe the cathodic process has been successfully optimized on the measured EIS data, and the kinetic parameters extracted from optimization to illustrate the passive film characteristics of HDSS 2707.
3. The dominating point defects within the passive film of HDSS 2707 are the cation interstitial (M_i^{n+}), $M = Cr$, Fe, and Ni, rendering the barrier layer n-type electronic character, which is in accordance with M-S measurements.
4. Both the diffusion coefficient (D) and the rate constant (k_i) of point defects are potential-independent at a given temperature, with latter being a constant, as determined by $a_i V + b_i L_{ss} =$ -G, based on PDM; but both increase with the temperature.
5. Both the passive current density and the thickness of the barrier layer increase with the increasing of temperature. The increment of barrier layer thickness is attributed to the suppression of the electric field strength by the thermal excitation of electrons and electron hole pairs. While the passive current density is independent of the quantum mechanically tunneling of charge carriers through the barrier layer; the kinetics of the partial cathodic reaction of hydrogen evolution is affected because of the voltage dependence of the barrier layer thickness and hence of the tunneling probability. Modeling of this process as part of the optimization of the MPM on the experimental EIS data yields corrected exchange current density and Tafel constant for the HER on the hypothetical bare metal surface.
6. The variation of anodic current density and the corresponding CR with temperature obey the Arrhenius law, i.e., $ln(CR) = 10.75 - 3825.54/T$, implying that the corrosion is a thermally activated process.
7. The passive current density of HDSS 2707 is found to be independent to applied voltage, while the thickness of the barrier layer increases linearly with the film formation potential ($L_{ss} = 2.89 + 2.91\ V_{SCE}$), as predicted by the PDM, for the case where no change in cation oxidation state occurs upon barrier layer dissolution or cation ejection.

CRediT authorship contribution statement

Li Sun: Conceptualization, Methodology, Experiment, Data curation, Writing. **Tianyu Zhao:** Data curation, Editing. **Jie Qiu:** Methodology, Editing. **Yangting Sun:** Conceptualization, Supervision, Project administration, Editing. Editing. **Weihua Li:** Editing. **Haibing Zheng:** Editing. **Zhifeng Lin:Si Chen:** Experiment. **Yiming Jiang:** Data curation, Editing. **Jin Li:** Data curation. **Digby D. Macdonald:** Methodology, Data curation, Editing, Supervision.

Declaration of Competing Interest

The authors declare that they have no known competing financial interests or personal relationships that could have appeared to influence the work reported in this paper.

Acknowledgments

This study is financially supported by the National Natural Science Foundation of China (Grant nos. 52071082, 51901046 and 51879292), and the China Scholar Fund who supported Li Sun and Tianyu Zhao during their stay at the University of California at Berkeley as Visiting Scholar in Professor Digby. D. Macdonald's research group.

References

[1] B. Zhang, Z. Jiang, H. Li, S. Zhang, H. Feng, H. Li, Precipitation behavior and phase transformation of hyper duplex stainless steel UNS S32707 at nose temperature, Mater. Charact. 129 (2017) 31–39.
[2] S.-H. Jeon, D.H. Hur, H.-J. Kim, Y.-S. Park, Effect of Ce addition on the precipitation of deleterious phases and the associated intergranular corrosion resistance of 27Cr–7Ni hyper duplex stainless steels, Corros. Sci. 90 (2015) 313–322.
[3] J. Wang, W.-l Chen, H.-j Meng, Y.-s Cui, C.-l Zhang, Influence of sigma phase on corrosion and mechanical properties of 2707 hyper-duplex stainless steel aged for short periods, J. Iron Steel Res. Int. 26 (2019) 452–461.
[4] V.A. Hosseini, K. Hurtig, L. Karlsson, Bead by bead study of a multipass shielded metal arc-welded super-duplex stainless steel, Weld. World 64 (2020) 283–299.
[5] L. Sun, Y. Sun, C. Lv, Y. Liu, N. Dai, Y. Jiang, J. Li, D.D. Macdonald, Studies on the degree of sensitization of hyper-duplex stainless steel 2707 at 900°C using a modified DL-EPR test, Corros. Sci. (2021), 109432.
[6] P.N. Raj, A.P. Sivan, K. Sekar, M. Joseph, Effect of austenite reformation on localized corrosion resistance of hyper-duplex stainless steel in hot chloride solution, Int. J. Metalcasting 14 (2020) 167–178.
[7] L. Sun, Y. Sun, Y. Liu, N. Dai, J. Li, Y. Jiang, Effect of annealing temperature on pitting behavior and microstructure evolution of hyper-duplex stainless steel 2707, Mater. Corros. 70 (2019) 1682–1692.
[8] D.D. Macdonald, The point defect model for the passive state, J. Electrochem. Soc. 139 (1992) 3434.

[9] M. Gholami, M. Hoseinpoor, M.H. Moayed, A statistical study on the effect of annealing temperature on pitting corrosion resistance of 2205 duplex stainless steel, Corros. Sci. 94 (2015) 156–164.
[10] J. Gao, Y. Jiang, B. Deng, W. Zhang, C. Zhong, J. Li, Investigation of selective corrosion resistance of aged lean duplex stainless steel 2101 by non-destructive electrochemical techniques, Electrochim. Acta 54 (2009) 5830–5835.
[11] J. Nilsson, A. Wilson, Influence of isothermal phase transformations on toughness and pitting corrosion of super duplex stainless steel SAF 2507, Mater. Sci. Technol. 9 (1993) 545–554.
[12] V. Maurice, W. Yang, P. Marcus, X-Ray photoelectron spectroscopy and scanning tunneling microscopy study of passive films formed on (100) Fe-18Cr-13Ni single-crystal surfaces, J. Electrochem. Soc. 145 (1998) 909.
[13] P. Marcus, V. Maurice, H.-H. Strehblow, Localized corrosion (pitting): a model of passivity breakdown including the role of the oxide layer nanostructure, Corros. Sci. 50 (2008) 2698–2704.
[14] A. Kolics, J. Polkinghorne, A. Wieckowski, Adsorption of sulfate and chloride ions on aluminum, Electrochim. Acta 43 (1998) 2605–2618.
[15] P. Natishan, W. O'grady, Chloride ion interactions with oxide-covered aluminum leading to pitting corrosion: a review, J. Electrochem. Soc. 161 (2014) C421.
[16] L. Sun, T. Zhao, J. Qiu, Y. Sun, K. Li, H. Zheng, Y. Jiang, Y. Li, J. Li, W. Li, D. D. Macdonald, Point defect model for passivity breakdown on hyper-duplex stainless steel 2707 in solutions containing bromide at different temperatures, Corros. Sci. (2021), 109959.
[17] G. Ou, K. Wang, J. Zhan, M. Tang, H. Liu, H. Jin, Failure analysis of a reactor effluent air cooler, Eng. Fail. Anal. 31 (2013) 387–393.
[18] G. Ou, H. Jin, H. Xie, J. Cao, J. Qiu, Prediction of ammonium salt deposition in hydroprocessing air cooler tubes, Eng. Fail. Anal. 18 (2011) 1458–1464.
[19] L. Sun, M. Zhu, G. Ou, H. Jin, W. Kai, K. Wang, Corrosion investigation of the inlet section of REAC pipes in the refinery, Eng. Fail. Anal. 66 (2016) 468–478.
[20] Z. Zheng, G. Ou, Y. Yi, G. Shu, H. Jin, C. Wang, H. Ye, A combined numerical-experiment investigation on the failure of a pressure relief valve in coal liquefaction, Eng. Fail. Anal. 60 (2016) 326–340.
[21] M.G. Lioliou, B. Kaasa, S. Berg, Modelling of Liquid-vapor-solid Equilibria in the NH3-CO2-H2O System.
[22] R. API, 932-B, Design Materials, Fabrication, Operation and Inspection Guidelines for Corrosion Control in Hydroprocessing Reactor Effluent Air Cooler (REAC) Systems, American Petroleum Institute (API), USA, 2012.
[23] C. Chao, L. Lin, D. Macdonald, A point defect model for anodic passive films: I. Film growth kinetics, J. Electrochem. Soc. 128 (1981) 1187.
[24] D.D. Macdonald, S.R. Biaggio, H. Song, Steady-state passive films: interfacial kinetic effects and diagnostic criteria, J. Electrochem. Soc. 139 (1992) 170.
[25] D.D. Macdonald, J. Qiu, S. Sharifi-Asl, J. Yang, G.R. Engelhardt, Y. Xu, E. Ghanbari, A. Xu, A. Saatchi, D. Kovalov, Pitting of carbon steel in the synthetic concrete pore solution, Mater. Corros. 72 (2021) 166–193.
[26] D.D. Macdonald, The history of the point defect model for the passive state: a brief review of film growth aspects, Electrochim. Acta 56 (2011) 1761–1772.
[27] J. Qiu, Y. Li, Y. Xu, A. Wu, D.D. Macdonald, Effect of temperature on corrosion of carbon steel in simulated concrete pore solution under anoxic conditions, Corros. Sci. 175 (2020), 108886.
[28] J. Yang, Y. Li, A. Xu, B. Fekete, D.D. Macdonald, The electrochemical properties of alloy 690 in simulated pressurized water reactor primary water: effect of temperature, J. Nucl. Mater. 518 (2019) 305–315.
[29] S. Sharifi-Asl, M.L. Taylor, Z. Lu, G.R. Engelhardt, B. Kursten, D.D. Macdonald, Modeling of the electrochemical impedance spectroscopic behavior of passive iron using a genetic algorithm approach, Electrochim. Acta 102 (2013) 161–173.
[30] D. Ribeiro, C. Souza, J. Abrantes, Use of electrochemical impedance spectroscopy (EIS) to monitoring the corrosion of reinforced concrete, Rev. IBRACON Estrut. Mater. 8 (2015) 529–546.
[31] X. Liu, J. Xiong, Y. Lv, Y. Zuo, Study on corrosion electrochemical behavior of several different coating systems by EIS, Prog. Org. Coat. 64 (2009) 497–503.
[32] A. Sun, J. Franc, D.D. Macdonald, Growth and properties of oxide films on platinum: I. EIS and X-ray photoelectron spectroscopy studies, J. Electrochem. Soc. 153 (2006) B260.
[33] D.D. Macdonald, Reflections on the history of electrochemical impedance spectroscopy, Electrochim. Acta 51 (2006) 1376–1388.
[34] E. Ghanbari, A. Saatchi, X. Lei, D.D. Macdonald, Studies on pitting corrosion of Al–Cu–Li alloys part III: passivation kinetics of AA2098–T851 based on the point defect model, Materials 12 (2019) 1912.
[35] P. Lu, B. Kursten, D.D. Macdonald, Deconvolution of the partial anodic and cathodic processes during the corrosion of carbon steel in concrete pore solution under simulated anoxic conditions, Electrochim. Acta 143 (2014) 312–323.
[36] J. Yang, Y. Li, D.D. Macdonald, Effects of temperature and pH on the electrochemical behaviour of alloy 600 in simulated pressurized water reactor primary water, J. Nucl. Mater. 528 (2020), 151850.
[37] D.D. Macdonald, J. Qiu, S. Sharifi-Asl, J. Yang, G.R. Engelhardt, Y. Xu, E. Ghanbari, A. Xu, A. Saatchi, D. Kovalov, Pitting of carbon steel in the synthetic concrete pore solution, Mater. Corros. (2020).
[38] D.D. Macdonald, M. Urquidi-Macdonald, Distribution functions for the breakdown of passive films, Electrochim. Acta 31 (1986) 1079–1086.
[39] D.D. Macdonald, PassivityÐthe key to our metals-based civilization, Pure Appl. Chem. 71 (1999) 951–978.
[40] D.D. Macdonald, M. Urquidi-Macdonald, Theory of steady-state passive films, J. Electrochem. Soc. 137 (1990) 2395.
[41] D.D. Macdonald, On the existence of our metals-based civilization: I. Phase-space analysis, J. Electrochem. Soc. 153 (2006) B213.
[42] D.D. Macdonald, J. Qiu, Re-defining the kinetics of redox reactions on passive metal surfaces, J. Solid State Electron. (2020) 1–15.
[43] P. Lu, S. Sharifi-Asl, B. Kursten, D.D. Macdonald, The irreversibility of the passive state of carbon steel in the alkaline concrete pore solution under simulated anoxic conditions, J. Electrochem. Soc. 162 (2015) C572.
[44] J. Bao, D.D. Macdonald, Oxidation of hydrogen on oxidized platinum: part I: The tunneling current, J. Electroanal. Chem. 600 (2007) 205–216.
[45] D. Macdonald, G. Englehardt, The point defect model for bi-layer passive films, ECS Trans. 28 (2010) 123.
[46] A. Sadkowski, J.-P. Diard, C. Montella, Problem of Kramers–Kroenig transformation of EIS data in case of instabilities, J. Electrochem. Soc. 156 (2008) F7.
[47] D.D. Macdonald, Review of mechanistic analysis by electrochemical impedance spectroscopy, Electrochim. Acta 35 (1990) 1509–1525.
[48] D.D. Macdonald, The passive state in our reactive metals-based civilization, Arab. J. Sci. Eng. 37 (2012) 1143–1185.
[49] J. Yao, D.D. Macdonald, C. Dong, Passive film on 2205 duplex stainless steel studied by photo-electrochemistry and ARXPS methods, Corros. Sci. 146 (2019) 221–232.
[50] D.D. Macdonald, M. Urquidi-Macdonald, Application of Kramers-Kronig transforms in the analysis of electrochemical systems: I. Polarization resistance, J. Electrochem. Soc. 132 (1985) 2316.
[51] M. Urquidi-Macdonald, S. Real, D.D. Macdonald, Application of Kramers-Kronig transforms in the analysis of electrochemical impedance data: II. Transformations in the complex plane, J. Electrochem. Soc. 133 (1986) 2018.
[52] M. Urquidi-Macdonald, S. Real, D.D. Macdonald, Applications of Kramers—Kronig transforms in the analysis of electrochemical impedance data—III. Stability and linearity, Electrochim. Acta 35 (1990) 1559–1566.
[53] L.G. McMillion. Defining the Passive State of Alloy 22 Using Electrochemical Impedance Spectroscopy and Deterministic Modeling, University of Nevada, Reno, 2005.
[54] S. Sharifi-Asl, D.D. Macdonald, A. Almarzooqi, B. Kursten, G.R. Engelhardt, A comprehensive electrochemical impedance spectroscopic study of passive carbon steel in concrete pore water, J. Electrochem. Soc. 160 (2013) C316.
[55] Z. Lu, D.D. Macdonald, Transient growth and thinning of the barrier oxide layer on iron measured by real-time spectroscopic ellipsometry, Electrochim. Acta 53 (2008) 7696–7702.
[56] D.D. Macdonald, Some personal adventures in passivity—a review of the point defect model for film growth, Russ. J. Electrochem. 48 (2012) 235–258.
[57] C. Chao, L. Lin, D. Macdonald, A point defect model for anodic passive films: III. Impedance response, J. Electrochem. Soc. 129 (1982) 1874.
[58] E. Young, P. Stiphout, J. De Wit, n-Type behavior of chromium (III) oxide, J. Electrochem. Soc. 132 (1985) 884.
[59] E. Young, J. Gerretsen, J. De Wit, The oxygen partial pressure dependence of the defect structure of chromium (III) oxide, J. Electrochem. Soc. 134 (1987) 2257.
[60] A. Loucif, J.-P. Petit, Y. Wouters, Semiconducting behavior and bandgap energies of oxide films grown on alloy 600 under PWR simulated primary water conditions with different dissolved hydrogen contents, J. Nucl. Mater. 443 (2013) 222–229.
[61] Y. Zhang, D.D. Macdonald, M. Urquidi-Macdonald, G.R. Engelhardt, R.B. Dooley, Passivity breakdown on AISI Type 403 stainless steel in chloride-containing borate buffer solution, Corros. Sci. 48 (2006) 3812–3823.
[62] J. Qiu, D.D. Macdonald, Y. Xu, L. Sun, General corrosion of carbon steel in a synthetic concrete pore solution, Mater. Corros. 72 (2021) 107–119.